Bruna B. Carvalho (bruna.borgescarvalho@unipd.it)

Into the high to ultrahigh temperature melting of Earth's crust: Investigation of melt and fluid inclusions within Mg–rich metapelitic granulites from the Mather Peninsula, East Antarctica

Zhao Liu [1], Bruna B. Carvalho [2], Wancai Li [3], Laixi Tong [1,*], Omar Bartoli [2], Longyao Chen [4], Qinghe Yan [5], Haobo Wu [1]

[1] State Key Laboratory of Continental Dynamics, Department of Geology, Northwest University, Xi'an 710069, China

[2] Dipartimento di Geoscienze, Università di Padova, Via Gradenigo 6, Padua 35131, Italy

[3] CAS Key Laboratory of Crust–Mantle Materials and Environments, School of Earth and Space Sciences, University of Science and Technology of China, Hefei 230026, China

[4] Key Laboratory of Paleomagnetism and Tectonic Reconstruction of Ministry of Natural Resources, Institute of Geomechanics, Chinese Academy of Geological Sciences, Beijing 100081, China

[5] School of Resource Environment and Earth Science, Yunnan University, Kunming 650091, China

Manuscript submitted to *Journal of Petrology*

(August 1st, 2022)

(*corresponding author: tonglx@nwu.edu.cn)

ABSTRACT

Precise constraints on the compositions of melts generated by anatexis under ultrahigh temperature (*UHT*) conditions are critical for understanding processes of partial melting and differentiation of the Earth's crust. Here we reveal geochemical and physical signatures of anatectic melts preserved as nanogranitoids (i.e. crystalized melt inclusions) within sapphirine–bearing *UHT* metapelitic granulites from the Mather Peninsula, East Antarctica. Their coexistence with high−Al orthopyroxene as inclusions in garnets strongly suggests that the investigated melts were at least partially *UHT* in origin. The nanogranitoids are enriched in SiO_2 (69.9−75.6 wt.%), strongly peraluminous (ASI values = 1.2−1.6) and potassic to ultrapotassic ($Na_2O + K_2O$ = 7.1−9.5 wt.%, K/Na = 2.2−9.3). When compared to the granulitic restite, the melts are enriched in Li, Cs, Rb, Ta, Sm, Nd, Zr, U and Pb, and depleted in Ce, Th, Ba, Sr and Nb. Their geochemical characteristics are consistent with biotite−dehydration melting in the absence of plagioclase. Our calculation results indicate that these hot crustal melts have low densities of 2.47 ± 0.07 g/cm^3, low viscosities of $10^{4.9\pm1.2}$ Pa·s and high heat production values of ~2.8 μW/m^3. Therefore, such melts are mobile and susceptible to be extracted from the source, and consequently their flow and removal from the deep crust may greatly affect the chemical and thermal structure of the continental crust.

Secondary C−O−H fluid inclusions within garnet and orthopyroxene have also been detected. These inclusions contain magnesite, pyrophyllite, corundum, with or without residual CO_2. The minerals within the fluid inclusions are interpreted as stepdaughter minerals, which were produced by the reaction of the fluid with their host. The metamorphic timing of the investigated rocks is still a matter of debate. Zircon U−Pb dating results obtained in this study suggest that the metapelitic granulites may have undergone two separated thermal events at ~1000 and ~530 Ma, respectively. The presence of fluid inclusions indicates that fluid infiltration and Pan–African reworking may have played an important role in obscuring chronological information of the early thermal scenario in poly–metamorphic terranes.

Key Words:

UHT metamorphism; Melt inclusions; C–O–H fluid; Mather Peninsula; East Antarctica

INTRODUCTION

Ultrahigh temperature (*UHT*) metamorphism is the most thermally extreme type of crustal metamorphism, with peak temperatures exceeding 900 ℃ at moderate pressures (7–13 kbar) (Harley, 1998a, 2008), with *dT/dP* values of 66–200 ℃/kbar (Harley, 2021). *UHT* metamorphism is now recognized as a relatively common rather than anomalous process of the Earth's crust due to 1) its wide age distribution ranging from Archean to Quaternary (e.g. Brown, 2007; Harley, 2021; Pownall et al., 2014; Zhang et al., 2022); and 2) its extensive exposures around the world (>70 localities; Harley, 2021; Lei & Xu, 2018) related to various geodynamic processes. For example, *UHT* metamorphism may occur in tectonic backgrounds associated with 1) lithospheric extension and underplating of mantle–derived magmas as a result of slab rollback (e.g. Pownall et al., 2014), mantle plume activity (e.g. Liu et al., 2020; Tong et al., 2014a); 2) oceanic ridge subduction (e.g. Santosh et al., 2012), and inversion and thickening of hot back–arc (e.g. Brown, 2007); 3) long–lived orogenic self–heating by radioactive elements (e.g. Clark et al., 2011; Zhang et al., 2022); or 4) a combined contribution from several driving forces (Huang et al., 2019, 2021).

High temperature (*HT*) to *UHT* metamorphism of crustal rocks inevitably produces anatectic melts at depth, and their loss yields a refractory lower crust, whereas ascent and emplacement of granitic melts at shallower levels create a more silicic upper crust (e.g. Brown, 2007, 2013; Sawyer et al., 2011). Furthermore, it may result in decrease of the rock strength and variations in bulk compositions of the granulitic rocks (e.g. Cavalcante et al., 2016; Diener & Fagereng, 2014; Rosenberg & Handy, 2005). However, interpretations of melting mechanisms of crustal rocks remain a long–standing challenge, which have been traditionally tracked with the aid of 1) geochemistry of granites and leucosomes (e.g. Gao et al., 2017; Wolf et al., 2019; Zeng et al., 2005), 2) phase equilibria modeling at specific *P–T* conditions (e.g. Huang et al., 2021; Wei, 2016; White et al., 2004, 2014), and 3) melting experiments on natural rocks under variable $P–T–X_{H2O}$ conditions (refer to Gao et al., 2016 and references therein). Furthermore, a recent progress is to conduct in–situ observations and analyses on nanogranitoid inclusions (partially to totally crystallized melt inclusions preserved in peritectic phases; named after Cesare et al., 2015) and their glassy counterparts (e.g. Acosta–Vigil et al., 2010, 2012; Bartoli et al., 2013a, b, 2014, 2016, 2019; Bartoli & Carvalho, 2021; Borghini et al., 2018, 2023; Carvalho et al., 2019, 2023a; Cesare et al., 2009, 2015; Ferrero et al., 2012, 2016, 2018, 2021a, b; Ferrero & Angel, 2018; Ferri et al., 2020;

Gao et al., 2014; Gianola et al., 2021; Higashino & Kawakami, 2022; Tacchetto et al., 2021). Thus far, melt inclusions have been only recognized in a few *UHT* metapelitic terranes, including 1) the Ivrea Zone (NW Italy) (Carvalho et al., 2019), 2) the Kerala Khondalite Belt (India) (Cesare et al., 2009; Ferrero et al., 2012), 3) the Gruf Complex (European Central Alps) (Gianola et al., 2021), 4) the Lützow–Holm Complex (East Antarctica) (Carvalho et al., 2023a; Hiroi et al., 2019; Kawakami & Motoyoshi, 2004; Suzuki & Kawakami, 2019), 5) the Sør Rondane Mountains (East Antarctica) (Higashino & Kawakami, 2022), and 6) the Chinese Altai orogen (NW China) (Liu et al., 2020). It is worth noting that the occurrence of nanogranitoids in *UHT* rocks does not imply automatically that they reflect the *UHT* crustal melts because melts can be trapped during the *HT* prograde metamorphism (refer to Gianola et al., 2021). A better understanding of potential effects of *UHT* metamorphism on the differentiation and dynamic evolution of the crust demands that the hottest crustal melts are chemically characterized, in particular for their major and trace elements.

The Mather metapelitic granulites from the Rauer Islands (East Antarctica) are a world–renowned poly−metamorphic *UHT* lithology, with peak *P–T* conditions of 8.5−12 kbar and 950–1050 °C (Chen et al., 2023; Clark et al., 2019; Harley, 1998b, 2016; Harley et al., 2009; Harley & Fitzsimons, 1991; Kelsey et al., 2007; Tong & Wilson, 2006). In this contribution, we conduct an integrated investigation of microstructural features, major and trace element contents of nanogranitoid inclusions (NIs) preserved within garnet porphyroblasts. Data collected in this work are fundamental to the understanding of melting regimes of crustal rocks under *UHT* conditions, and their contribution to crustal differentiation and orogenic evolution. Secondary fluid inclusions (FIs) in peritectic phases are also characterized to reveal the nature of post−peak infiltrated fluid, and to evaluate its potential role in resetting the U–Pb clock of zircons.

GEOLOGICAL SETTING

The Antarctic continent is separated by the Transantarctic Mountains into two distinct geological units, namely East Antarctica and West Antarctica. East Antarctica is one of the largest cratons around the world, documenting more than 3.5 billion years of evolutional history (Harley et al., 2013). The Prydz Belt was recognized as a tectonic mobile belt in East Antarctica that has been extensively affected by the Pan–African (~530 Ma) thermal event (e.g. Grew et al., 2012; Harley et al., 1998; Harley & Kelly, 2007; Hensen & Zhou, 1997; Kelsey et al., 2003, 2007; Liu et al., 2009,

2021; Tong et al., 2014b, 2019; Wang et al., 2007, 2008, 2022). The tectonic nature of the Prydz Belt remains debated and there are two main schools of thought; one considers that it represents a Pan–African suture zone associated with the final assembly of East Gondwana (e.g. Fitzsimons, 2003; Hensen & Zhou, 1997; Kelsey et al., 2007; Liu et al., 2021; Wang et al., 2022; Zhao et al., 1995), and the other views it as a Pan–African intraplate orogen related to intracontinental reworking (e.g. Phillips et al., 2007; Ren et al., 2016; Tong et al., 2014b, 2019; Wilson et al., 2007).

The Rauer Islands are located on the eastern margin of the Prydz Belt, with the Brattstrand Bluff and Larsemann Hills to the southwest, and the Vestfold Hills to the northeast. The Rauer Islands were thought to be texturally correlated with the Rengali–Eastern Chats Province, forming parts of the Indo–Antarctica supercontinent (e.g. Sawant et al., 2017). Archean and Proterozoic crustal components have been recognized from the Rauer Islands (Kinny et al., 1993). The Proterozoic domain comprises metamorphosed 1420–1000 Ma mafic–intermediate–felsic intrusive rocks (Kinny et al., 1993; Liu et al., 2021). The early Neoproterozoic (i.e. Grenville–aged; 1000–900 Ma) and late Neoproterozoic/Cambrian (i.e. Pan–African–aged; 590–500 Ma) ages have been identified from metamorphic rocks in this region (e.g. Kelsey et al., 2007; Kinny et al., 1993; Liu et al., 2021). The Archean domain predominantly consists of tonalitic to granitic orthogneisses with three age clusters of 3470–3270, 2840–2800 and ~2550 Ma (Harley et al., 1998; Hokada et al., 2016; Kinny et al., 1993; Liu et al., 2021). This domain also contains Fe– or Mg–rich layered mafic complexes that were subjected to a granulite facies metamorphism in the Cambrian (Chen et al., 2023; Harley et al., 1998; Harley & Kelly, 2007). Although Pan–African ages have been widely recognized in the Archean domain (e.g. Clark et al., 2019; Hokada et al., 2016; Kelsey et al., 2003, 2007; Liu et al., 2021; Wang et al., 2007), it is still unclear whether it was also involved in the Grenville–aged tectono–thermal event.

The Rauer Islands consist of two paragneiss successions, namely the Filla and the Mather Paragneisses (Fig. 1a; Harley & Fitzsimons, 1991). These two paragneiss successions are mainly distributed on the Proterozoic and Archean crustal domains, respectively. Deposition ages of the Filla Paragneiss have been constrained to be Mesoproterozoic (Liu et al., 2021; Sims et al., 1994). This unit was considered to have experienced a prominent metamorphic event at 1030–970 Ma and a high–grade reworking at 575–510 Ma (e.g. Kelsey et al, 2007; Kinny et al., 1993; Liu et al., 2021). The Mather Paragneiss typically comprises magnesian and aluminous garnet–orthopyroxene–

sillimanite–bearing metapelite, orthopyroxene–sillimanite metaquarzite, magnesian garnet–orthopyroxene metapelite and garnet–bearing mafic granulite (Fig. 1b; Harley et al., 1995; Harley, 1998b). This suite usually occurs as thin and laterally discontinuous horizons from the Mather Peninsula to the Short Point in the eastern Rauer Islands (Hokada et al., 2016). Mather Paragneiss preserves strong evidence for *UHT* metamorphism, with exposures of sapphirine–bearing metapelitic granulites on the Mather Peninsula (e.g. Harley, 1998b; Tong & Wilson, 2006) and the Torckler Island (Harley et al., 2009), with peak *P–T* conditions of 8.5–12 kbar and 1000–1050 ℃ (e.g. Harley, 1998b, 2016; Tong & Wilson, 2006). The sapphirine–bearing *UHT* gneisses preserve inherited zircon ages of 2800–2400 Ma (e.g. Hokada et al., 2016; Wang et al., 2007), and are hosted by ~3267 Ma tonalitic orthogneisses (Hokada et al., 2016). However, timing of the *UHT* metamorphism is still a matter of debate. Some researchers argued that the *UHT* metamorphism occurred at ~1000 Ma and the subsequent decompression and final cooling happened at ~530 Ma (e.g. Tong & Wilson, 2006; Wang et al., 2007) while others considered that the *UHT* metamorphism occurred in the Cambrian (e.g. Clark et al., 2019; Kelsey et al., 2003, 2007) or prior to 590–580 Ma (Hokada et al., 2016; Harley et al., 2009).

PETROGRAPHY

The granulite sample RG16–80 (68°50’50’’ S and 77°54’43’’ E) was collected from the Mather Peninsula in the Rauer Islands, East Antarctica (Fig. 1b). Compositions and mineral assemblages vary considerably at outcrop scale, ranging from quartz–bearing to SiO_2–undersaturated rocks (refer to Harley, 1998b for more details). The studied rocks occur as discrete rafts or boudins interlayering with Grt–Opx–Sil–Spr granulites, Grt–rich quartzites, Grt–Sil metapelites, two–pyroxene granulites, Opx–Sil–(Per)–bearing and Spr–Opx–Kfs–bearing leucogneisses (Fig. 2). Mineral abbreviations are from Warr. (2021). The studied Mg−rich metapelites constitute 5–8% of the outcrop, and are roughly parallel to foliation S6 (Tong & Wilson, 2006), corresponding to the composite high−strain fabric described by Dirks & Wilson (1995). The samples are coarse–grained, with an assemblage of orthopyroxene (35–45%), biotite (25–30%), garnet (~15%), cordierite (7–10%), minor sapphirine, plagioclase, K–feldspar, quartz (<5%), and accessory spinel, ilmenite, apatite, zircon and monazite (Fig. 3).

Garnet porphyroblasts are subhedral to anhedral, with sizes varying from 0.1 to 30 mm. They

usually preserve corroded biotite and quartz inclusions in cores. Most orthopyroxene grains are present as porphyroblasts (up to 1.2 cm in diameter), and in rare cases, they may contain platy or rounded biotite inclusions (Figs. 3a, b). The inclusions within garnet cores and orthopyroxene, such as biotite and quartz, are considered as pre–peak (M0) minerals. The cores of orthopyroxene porphyroblasts are considered to have been formed at M0 stage because they contain relatively low Al_2O_3 contents (<6.5 wt.%) compared with the rim (>8.0 wt.%; Opx_1) (see details on the section of mineral chemistry), and high Al_2O_3 contents in orthopyroxene usually suggest that they were formed under *UHT* conditions (e.g. Harley, 1998a).

Sometimes, orthopyroxene with high Al_2O_3 contents (up to 8.85−9.04 wt.%) may occur as inclusions within garnet mantle (Fig. 3a), and both minerals are considered to form at, or close to, peak conditions. Collectively, garnet mantles, orthopyroxene rims, high−Al orthopyroxene inclusions within garnets and biotite porphyroblasts (Fig. 3b) are interpreted to be formed at the metamorphic peak (M1) stage. K–feldspar occurs in very local domains, and is usually 0.5–4.0 mm in size (Fig. 3c). However, it is difficult to determine whether K–feldspar was formed at M0 or M1 stage based on petrographic observations.

The presence of biotite and quartz inclusions within garnets, coupled with the formation of garnet and orthopyroxene porphyroblasts, implies the progress of the following Bt−dehydration melting reaction:

Bt (+ Kfs) + Qz → Grt + Opx + melt.

Garnet porphyroblasts are commonly replaced at their margins by the intergrowth of orthopyroxene (Opx_2) + cordierite ± biotite ± plagioclase ± spinel (Figs. 3d, e), which are assigned to the post−peak (M2) assemblage. Formation of the intergrowth is considered to result from the following decompression−related reaction:

Grt → Opx_2 + Crd ± Spl (e.g. Harley, 1998b; Santosh et al., 2012).

Intergrowths of sapphirine + cordierite are found in the matrix (Fig. 3f). Occasionally, vermicular low–Al orthopyroxene and plagioclase are preserved in the rim of high–Al orthopyroxene porphyroblasts (Fig. 3g). These microstructures are also interpreted to form at the post−peak (M2) stage.

Some medium– to fine–grained sapphirine strips are associated with oriented biotite, which sometimes, may surround orthopyroxene + cordierite intergrowths (Fig. 3h). In strongly deformed

domains, elongated garnet, cordierite, biotite, plagioclase, rare orthopyroxene and spinel grains show a similar orientation (Fig. 3i), which may have been formed at the final cooling (M3) stage. The appearance of interstitial plagioclase films suggests the presence of former melts (Fig. 3i) (e.g. Holness et al., 2011).

The presence of retrograde biotite and plagioclase is in agreement with progress of the following reaction:

Grt (Opx) + melt → Bt + Pl ± Qz.

In summary, the Spr–bearing *UHT* granulites (sample RG16−80) from the Mather Peninsula preserve four–stage metamorphic assemblages: 1) M0 stage is represented by the Bt–Qz–bearing inclusions and the cores of garnet and orthopyroxene porphyroblasts; 2) M1 stage is marked by the growth of garnet–orthopyroxene$_1$−biotite in the presence of melt, with or without the presence of K−feldspar; 3) M2 stage is featured by the development of orthopyroxene$_2$ + cordierite ± biotitet ± plagioclase ± spinel and sapphirine + cordierite intergrowths surrounding the peak garnet or orthopyroxene; and 4) M3 stage is characterized by the growth of cordierite–biotite—plagioclase–bearing assemblages during the crystallization of melts.

ANALYTICAL METHODS

Back–scattered electron imaging, X–ray mapping and EPMA analysis

Analyses of major elements in minerals and back–scattered electron (BSE) imaging were conducted using JEOL JXA–8230 electron probe microanalyzer (EPMA) at the Department of Geology, Northwest University, Xi'an, China. Additional X–ray mapping of NIs was done using JEOL JXA–8230 EPMA at the Wuhan Sample Solution Analytical Technology Co., Ltd., Wuhan, China. Analytical conditions were: an accelerating voltage of 15 kV, and a beam current of 2×10^{-8} A, a beam diameter of 2 μm. Counting times were 20 s on peaks, with 10 s on backgrounds. Data correction was processed by using a ZAF method. Fe^{3+} was calculated by charge balance. The analysis results are shown in Table 1. X–ray mapping was performed using an accelerating voltage of 20 kV, a beam current of 5×10^{-8} A, a beam diameter of 0.3 μm and a dwell time of 50 ms.

Trace elements in garnet

Trace element analyses of garnets were conducted with LA–ICP–MS at the Wuhan Sample Solution

Analytical Technology Co., Ltd., Wuhan, China. Detailed operating conditions of the laser ablation system, the ICP–MS instrument and the data reduction were as same as in Zong et al. (2017). Laser sampling was performed using a GeolasPro laser ablation system that consists of a COMPexPro 102 ArF excimer laser and a MicroLas optical system. An Agilent 7700e ICP–MS instrument was used to acquire ion–signal intensities. A "wire" signal smoothing device was included in this laser ablation system (Hu et al., 2015). Spot size and frequency of the laser were set to be 44 μm and 5 Hz, respectively. Trace element compositions of garnets were calibrated based on various reference materials (BHVO–2G, BCR–2G and BIR–1G) without using an internal standard (Liu et al., 2008). An Excel–based software ICPMSDataCal was used to perform quantitative calibration for trace element analyses (Liu et al., 2008).

Raman measurements

Micro–Raman measurements were performed on representative thick sections at the School of Earth Science and Resources, Chang'an University, using a HORIBA LabRam HR Raman microspectrometer. A frequency–doubled Nd:YAG laser with 532 nm excitation wavelength was used. A petrographic microscope Olympus (50 × objective) was used to focus the laser on the selected inclusions. Raman spectra in the ranges 100–4000 cm^{-1} were collected with an integration time of 10 s, and three accumulations. Data were processed using LabSpec v5.58.25 and the phases inside the inclusions were identified according to the data from the literature (Frezzotti et al., 2012; Ferrero et al., 2016, 2021b; Carvalho et al., 2020; Gianola et al., 2021).

Re–homogenization of nanogranitoids

Re–homogenization experiments of NIs were conducted following the procedure described in Bartoli et al. (2013a), using a piston cylinder apparatus at the CAS Key Laboratory of Crust–Mantle Materials and Environments, University of Science and Technology of China and the QUICKpress non−endloaded piston cylinder available at the Laboratory of Experimental Petrology and Geochemistry, Dipartimento di Geoscienze, Università di Padova. During each run, separated garnet grains were charged into Au capsules with external diameters of 3–5 mm and length of 5–10 mm. They were alternated by powdered silicon dioxide. The experiments were performed under the following conditions: 1000 ℃ and 6 hours, 950 ℃ and 4 hours, 950 ℃ and 2 hours, and 950 ℃ and

1 hour. A fixed pressure of 12 kbar was adopted during the experiments.

Major elements in nanogranitoids

Major element compositions of the re–homogenized NIs were determined using a JEOL JXA 8530F plus EPMA at the CAS Key Laboratory of Crust–Mantle Materials and Environments, University of Science and Technology of China, Hefei, China. During EMPA analysis of hydrous granitic glasses, migration and loss of alkali from the inclusions may happen in the case that small beam sizes and high beam currents are adopted (e.g. Cesare et al., 2015). To minimize the alkali loss, K_2O and Na_2O were determined at first. An anhydrous glass B (Morgan & London., 2005) was analyzed to obtain correction coefficients, which were used to correct the data of the unknown glasses. Analytical conditions were set as: a 15 kV accelerating voltage, a 5 nA beam current, variable beam diameters of 2–5 μm and counting times of 10 s on peak and 5 s on backgrounds.

Trace elements in nanogranitoids

Trace elements in NIs were analyzed at the State Key Laboratory for Mineral Deposit Research, Nanjing University, using a Coherent GeolasHD system equipped with a 193 nm excimer laser coupled to a NexION 350 ICP mass spectrometer (Pan et al., 2019). The samples were loaded and analyzed in an in–house rhomb–shaped plexiglass cell of relatively small internal volume to enable fast washout of aerosol. The He–based aerosol was admixed with nebulizer gas via a T–junction prior to injection into the plasma. The ICP–MS was tuned to achieve maximum sensitivity and low oxide production rate by lowering the ThO/Th ratios to <0.5 % before analyses. The analyzed inclusions are 2–25 μm beneath the surface to ensure they were representative of the original melts. The NIs close to the surface (2–10 μm in depth) were preferentially selected for analyses. In the rare case of deep–seated inclusions (15–25 μm in depth), the host garnet next to the inclusion was also analyzed and the ablation signal from the same depth interval as the inclusion was integrated, which will minimize the down–hole fractionation of elements during ablation (Zajacz and Halter, 2007). Repetition rate of the laser was increased to 10 Hz, on−sample energy densities of 5 J/cm^2 and spot size of 24 or 32 μm based on the size of NIs. Generally, measurement of each melt inclusion consists of 20–30 s instrumental background followed by 50–80 s ablations depending on the depth of melt inclusion. The glass NIST SRM 610 was employed as external standard. For the analyses of

the NIST SRM 610, the spot size and energy density were set as 32 μm and 5 J/cm^2, respectively. The acquired time–resolved signals were processed using the software SILLS (Guillong et al., 2008). Due to the small size of NIs, part of the host garnet has also been ablated along with target inclusions. Therefore, deconvolution of the resulting mixed garnet–glass signal was applied following the procedures of Halter et al. (2002). The Al_2O_3 of the re–homogenized inclusions derived from EPMA was adopted as reference standards for inclusions and garnet hosts, and MgO was used as the matrix−only tracer. Uncertainties and calculated limits of detection increase with the concentrations of elements in the host, thus, some elements which are strongly compatible in the host garnets (e.g. Y, Gd, V, Zn, Sc and heavy rare earth elements−HREEs) are normally not detectable in the inclusions. Some inclusions show anomalously high concentrations of Zr, Th, U, Nb and Sr, suggesting the occurrence of accidental trapped phases (e.g. zircon, monazite, rutile and apatite) (Bartoli et al., 2019). For these inclusions with extremely high contents of Zr, Th, U, Nb and Sr, only Rb, Cs, Ba and Li are reported in Table 4 and discussed in the text.

U–Pb dating of zircon

Conventional magnetic and heavy liquid techniques followed by hand–picking under a binocular microscope were used for separation of zircons from the Mather *UHT* metapelitic granulites. Morphology and internal structure of the zircons were documented with transmitted, reflected light microphotographs and cathodoluminescene (CL) images. Zircon U–Pb dating was carried out using LA–ICP–MS at the Wuhan Sample Solution Analytical Technology Co., Ltd., Wuhan, China. Detailed operating conditions for the laser ablation system and the ICP–MS instrument and data reduction were described in Zong et al. (2017). Laser sampling was performed using a GeolasPro laser ablation system that consists of a COMPexPro 102 ArF excimer laser (wavelength of 193 nm and maximum energy of 200 mJ) and a MicroLas optical system. Each analysis incorporated a background acquisition of approximately 20–30 s followed by 50 s of data acquisition from the sample. Spot size and frequency of the laser for analyses were set to 24 mm and 10 Hz, respectively. Zircon 91500 and glass NIST610 were used respectively as external standards for U–Pb dating and trace element calibrations. In order to monitor the external uncertainties of zircon dating, a zircon standard GJ−1 was alternately analyzed together with the other unknown zircons. Fourteen measurements of the zircon GJ−1 yielded a weighted mean $^{206}Pb/^{238}U$ age of 602.1 ± 4.4 Ma

(MSWD = 0.22), which is roughly in agreement with the recommended $^{206}Pb/^{238}U$ age value of 600.4 ± 0.6 Ma (Jackson et al., 2004). An Excel–based software ICPMSDataCal was used to perform off–line selection and integration of background and analyzed signals, time–drift correction and quantitative calibration for trace element analyses and U–Pb dating (Liu et al., 2010). Programs SQUID 1.0 and ISOPLOT (V.3.0; Ludwig, 1999) were used for data processing.

RESULTS

Mineral Chemistry

Garnet porphyroblasts are chemically homogeneous from core to mantle ($Alm_{34–38}Prp_{59–62}Grs_{3–4}Sps_{0–1}$). Small garnet crystals and garnet porphyroblast rims have slightly lower pyrope contents, with compositions of $Alm_{40–46}Prp_{55–56}Grs_{4–3}Sps_{0–1}$ (Figs. 4a, b). The garnet relicts from the strongly deformed domain display the lowest magnesium contents ($Alm_{48–50}Prp_{46–44}Grs_{4–5}Sps_{0–1}$). NI–bearing and NI–absent domains display similar REE patterns in the chondrite–normalized diagram, with enrichments of HREEs and slightly negative Eu anomalies (Fig. 4c).

Orthopyroxene porphyroblasts preserve evident Al–zoning patterns, with y_{Al} (= Al^{IV}= Al/2) values increasing from 0.14 (Al_2O_3 = ~6.49 wt.%) in the core to 0.19 (Al_2O_3 = ~8.79 wt.%) in the rim (Fig. 4d). The highest Al_2O_3 content of orthopyroxene detected in the sample is ~9.16 wt.%, with corresponding y_{Al} value of 0.19. However, orthopyroxene porphyroblasts show relatively restricted X_{Mg} (X_{Mg} = Mg/(Mg + Fe^{2+})) variations (0.77–0.79). Orthopyroxene inclusions in garnet have Al_2O_3 contents of 8.85–9.04 wt.% (y_{Al} = ~0.19) and X_{Mg} values of 0.78–0.80. Orthopyroxene from the orthopyroxene–cordierite symplectites have y_{Al} of 0.14–0.16 and X_{Mg} of 0.75–0.80. Vermicular low–Al orthopyroxene in the rims of some orthopyroxene porphyroblasts displays Al_2O_3 contents of ~6.88 wt.% (y_{Al} = ~0.15) and X_{Mg} values of ~0.77. Orthopyroxene grains associated with the retrograde biotite display Al_2O_3 contents of 7.67–7.69 (y_{Al} = 0.16–0.17) and X_{Mg} of 0.74–0.76.

Biotite porphyroblasts show relatively homogeneous compositions, with TiO_2 contents of 4.29–4.61 wt.% and X_{Mg} of 0.79–0.81. The low TiO_2 contents for peak biotite can be partially ascribed to crystal–chemical constraints, which hamper the temperature control on Ti content of biotite (Cesare et al., 2008). Biotite inclusions within garnet have relatively higher X_{Mg} values (0.84–0.87) than those within orthopyroxene (~0.79). However, they show similar TiO_2 content variations ranging

from 2.90 to 4.46 wt.%. The retrograde biotite has TiO_2 contents of ~2.63 wt.% and X_{Mg} values of ~0.81. Halogen concentrations in the analyzed biotite crystals are undistinguishable, with F and Cl contents of 0.09−0.37 wt.% and 0.10−0.12 wt.%, respectively.

Sapphirine associated with retrograde biotite has slightly higher X_{Mg} values (0.84–0.86) than that from sapphirine–cordierite intergrowths (0.80–0.82), both of which show indistinguishable Fe^{3+}/Fe^{T} ratios varying from 0.71 to 0.81. Cordierite grains from different positions show restricted X_{Mg} variations from 0.90 to 0.92. Spinel has X_{Mg} of 0.43–0.48 and ZnO contents of 0.64–1.72 wt.%. Plagioclase from the orthopyroxene–cordierite intergrowths is rich in anorthite, with a typical X_{An} (= Ca/(Ca + Na + K)) of ~0.81. However, plagioclase associated with the retrograde biotite has lower X_{An} values of 0.51–0.58.

Microstructures of melt and fluid inclusions

Nanogranitoids are randomly distributed within garnet crystals, but absent in the outer rims (Figs. 3a, 4a, 5a). They are also absent in the small garnet crystals from the strongly deformed domains (Fig. 3i). These inclusions show spherical or polygonal shape, and are 5−15 μm in size (Figs. 5b–f, 6). They usually display negative crystal shapes, and may contain nano–scale porosities (Fig. 5e), implying the possible presence of fluid which was dissolved in the former melts and subsequently exsolved upon crystallization (Bartoli et al., 2013b). Coupled Raman analyses and compositional maps suggest that they contain daughter phases of quartz, kokchetavite ($KAlSi_3O_8$), minor kumdykolite ($NaAlSi_3O_8$) and biotite (Figs. 5g, 6), indicating the former presence of silicate melts. Moreover, an unknown phase with Raman peaks at 292, 429 and 476 cm^{-1} has also been detected (Fig. 5g). Such phase has been previously recognized within garnet−hosted melt inclusions from the Gruf Complex (Gianola et al., 2021) and the Central Maine Terrane (Ferrero et al., 2021b). This phase was described as phase “430” by Ferrero et al. (2021b). Apatite, rutile, zircon and monazite may be present as accidentally trapped phases, as indicated by the relatively large size of trapped phases compared with the size of the melt inclusions, and also by their low solubility in granitic melts (e.g. Bartoli et al., 2019). Daughter biotite crystals in NIs have very low TiO_2 contents of 0.03–0.50, and is characterized by high X_{Mg} values ranging from 0.92 to 0.95, whereas F and Cl contents in biotite are negligible, lower than 0.07 and 0.03 wt.%, respectively. Kokchetavite has a

typical composition of $Or_{94}Ab_6$ and kumdykolite displays compositions of $Or_5An_8Ab_{87}$. For detailed mineral compositions, please refer to Table 2.

Fluid inclusions are also found within garnet (Figs. 3a, 7a, b) and orthopyroxene (Fig. 7c). These fluid inclusions display granular or vermicular shapes, with sizes of 5–40 μm (Fig. 7). They are usually present along healed cracks, suggesting that they are secondary in origin. Some early trapped fluid has reacted with their hosts to produce stepdaughter phases (i.e. their precipitation results from fluid−host interaction; Carvalho et al., 2020) of pyrophyllite, magnesite, corundum and quartz, with or without residual CO_2 (Figs. 7d, e). The measured CO_2 Fermi diad splits range from 102.8 to 105.1 cm^{-1}, corresponding to densities of 0.2–1.0 g/cm^3 calculated with the densimeter of Wang et al. (2011). Secondary pure CO_2 inclusions may also occur along healed garnet cracks (Fig. 7f), which have a density of ~0.8 g/cm^3. Although not detected in this study, the existence of trace amounts of free H_2O cannot be precluded because H_2O–rich liquid may be present as a thin film (<0.1 μm) wetting the walls of the FIs at ambient conditions (e.g. Berkesi et al., 2009; Lamadrid et al., 2014). Other fluid species such as N_2 and CH_4 have not been detected in this study.

Microstructures of re−homogenized nanogranitoids

Experiments at 950 °C with run durations of 2–4 hours yielded some homogenized melt inclusions. However, those at 950 °C with run duration of 1 hour produced the largest proportion of perfectly re−homogenized inclusions (Fig. 8). Some inclusions show clear evidence for overheating, such as the occurrences of 1) irregular boundaries between inclusions and garnet hosts (Fig. 8a); 2) secondary minerals (i.e. orthopyroxene) formed during experiments or upon quenching (Figs. 8a–d); 3) new growth of garnet on the inclusion walls (Fig. 8c); and 4) offshoots around melt inclusions formed as a consequence of decrepitations (Figs. 8a, b). The compositions of these inclusions showing interaction with the host have been disregarded. Shrinkage bubbles have also been observed within the overheated inclusions (Figs. 8b, c), suggesting that the fluid may have undergone incomplete dissolution in the melts during the experimental run or, alternatively, it diffused during cooling to form shrinkage bubbles (Lowenstern, 1995; Bartoli et al., 2013a). Some inclusions were not re−homogenized properly during the experiments, as indicated by the coexistence of melts with rounded residual quartz (Fig. 8d). Some melt inclusions still contain accessory minerals such as apatite, rutile, zircon and monazite (Figs. 8a, d–f). This strongly

indicates that these phases are accidentally trapped minerals (Ferrero et al., 2012).

Major element compositions of re–homogenized nanogranitoids

Re–homogenized inclusions are strongly peraluminous (ASI = $[Al_2O_3/(CaO+Na_2O+K_2O)]$ = 1.24−1.61) (Fig. 9) and rhyolitic in composition, with high SiO_2 contents of 69.89−75.61 wt.%, high Na_2O+K_2O contents of 7.08−9.53 wt.% (K/Na = 2.21−9.31) and extremely low CaO (< 0.7 wt.%) and FeO+MgO contents (Table 3). Difference of EMPA totals from 100% suggest that the H_2O contents in the analyzed MIs are 1.49 to 4.24 wt.%, with an average value of 2.79 wt.%.

In the CIPW–normative Qz–Ab–Or diagram (Fig. 10a), the high–SiO_2, potassic to ultrapotassic melts plot far away from haplogranitic minimum melts, and define an elongated trend paralleling to the Qz–Or sideline, which are consistent with the melt compositions found in other *UHT* occurrences reported by Cesare et al. (2009), Gianola et al. (2021) and Ferrero et al. (2012). Similar compositions have also been obtained by melting experiments of pelitic protoliths at 5–7 kbar and 900–950 °C (Droop et al., 2003; Patiño Douce & Johnston, 1991) (Fig. 10a). In the Ab–An–Or diagram, the NIs show variable Or/Ab ratios and low An contents. They plot in the granite field, and are close to the boundary between granite and Qz–monzonite (Fig. 10b).

Trace element compositions of nanogranitoids

In the average upper continental crust (UCC) normalized diagram (Rudnick & Gao, 2014), NIs from the Mather Peninsula are enriched in Rb, Sm, Ta and depleted in Ba, Pb, Th, Ce and Sr (Fig. 11). Compared with the granulitic restite (i.e. granulites that have experienced partial melting and substantial melt loss), NIs are enriched in Li (5.3−76.9 ppm), Cs (0.9−35.5 ppm), Rb (126.7−1325.0 ppm), Ta (1.4–3.2 ppm), Sm (5.5−27.2 ppm), Zr (84.2−276.5 ppm), Nd (7.2–22.8 ppm), and depleted in Ce (2.4−13.4 ppm), Th (0.4−3.8 ppm), Ba (56.3−565.6 ppm), Sr (5.8−27.6 ppm) and Nb (4.0–15.7 ppm) (Table 4; Fig. 11). The melts have relatively higher U (0.6−9.3 ppm) and Pb contents (3.9−12.8 ppm), and display higher Rb/Sr (7.69−52.08) and Sm/Nd (0.52−1.14) ratios relative to the granulitic restite (Rb/Sr = ~8.56; Sm/Nd = ~0.25). They also contain variable amounts of Sc (9.7−42.0 ppm), V (29.4−146.6 ppm) and Zn (83.3–130.7 ppm), which are discarded in this study because these concentrations might be affected by contamination from the garnet hosts (Bartoli et al., 2019).

Zircon morphology, U–Pb dates and trace elements

Zircon grains from the Mather *UHT* metapelitic granulites are usually rounded, and have grain sizes of 80–250 μm. They typically display complex core–mantle–rim structures and occasionally, they may be homogeneous in the CL images (Fig. 12a). The cores are generally 30–120 μm in diameter, and show oscillatory zoning or homogeneous patterns. Most zircon cores are enclosed by dark–grey mantles, which usually show blurred zoning or are unzoned. Sometimes, zircon cores and mantles are enveloped by pale–grey to bright rims (Fig. 12a). A total of 46 analyses of zircon were conducted on 34 grains. Zircon cores yield inherited $^{207}Pb/^{206}Pb$ dates of 2623–2088 Ma (N = 13; Th/U = 0.28–1.81). Zircon mantles document $^{206}Pb/^{238}U$ dates ranging from 1050 to 607 Ma (N = 27; Th/U = 0.01–0.09) while the rims record $^{206}Pb/^{238}U$ dates varying from 569 to 472 Ma (N = 6; Th/U = 0.11–0.34) (Table 5).

Orthopyroxene, biotite, plagioclase, apatite, chlorite, quartz and monazite inclusions were observed within zircons (Fig. 12c). Some trivial inclusions are extensively present along the healed fractures in zircons (Figs. 12b, d). They cannot be analyzed due to their small sizes. However, their appearance resembles FIs reported in literature (Fig. 6d in Li et al., 2018). Thus, these inclusions are suspected to also be FIs. Accordingly, the large variations of U–Pb dates for zircon mantles and rims (Fig. 12e) and Pb loss could result from extensive fluid infiltration and the Pan–African *HT–UHT* overprinting. Zircon cores are characterized by the presence of low–Mg biotite (X_{Mg} = ~0.71) and low–Ca plagioclase (X_{An} = ~0.35) inclusions (Table 1), which were not found in the matrix, suggesting that these cores are detrital in origin. It is worth noting that an orthopyroxene grain enclosed in a detrital zircon (i.e. it shows a near concordant date of ~2381 Ma) shows high Al_2O_3 contents of ~6.79 wt.% (Fig. 12c), indicative of a possible high–grade metamorphism in the Paleoproterozoic.

PHASE EQUILIBRIA MODELING

Phase equilibria modeling for the Mather *UHT* metapelitic granulite sample (RG16−80) was conducted with Perple_X (v. 6.9.1; Connolly, 2005) and the ds622 thermodynamic data set (Holland & Powell, 2011). Pseudosections were calculated in the 11–component $MnO–Na_2O–CaO–K_2O–FeO–MgO–Al_2O_3–SiO_2–H_2O–TiO_2–O_2$ (MnNCKFMASHTO) system. This system is considered to provide a realistic approximation to the composition of the samples within which melt

and Fe^{3+} can be assessed. The solution model for sapphirine is from Wheller & Powell (2014) and *a–x* models for other phases are same to those adopted by White et al. (2014). Whole–rock composition of a piece of relatively homogeneous rock (5×5×3 cm^3), obtained from XRF analysis, was used as the bulk rock composition for the modeling. The formation of fine–grained intergrowths is usually controlled by local effective bulk compositions. In this study, we assume that whole–rock composition obtained from XRF can roughly represent the local effective bulk composition of the symplectite formation. The H_2O contents were adjusted to ensure that the final assemblage is stable just above the solidus (Korhonen et al., 2012). A preliminary T–X(Fe_2O_3) diagram was calculated to evaluate the effect of Fe^{3+}contents on phase assemblage (Supplementary file). Based on the predicted peak assemblages across the range of Fe^{3+} contents, a Fe^{3+}/Fe^{T} value of ~0.16 is finally adopted.

Peak and post−peak evolution of the Mather *UHT* metapelitic granulites

A pseudosection for the rocks was constructed within a *P–T* window of 3–15 kbar and 750–1200 ℃. Due to lower diffusion rates of Al^{3+} compared to Fe^{2+} and Mg^{2+}, aluminum contents in orthopyroxene are considered reliable to document the peak temperatures of *UHT* metamorphism. As shown in Figure 13a, the pseudosection is contoured by (X_{Mg}(Opx) = Mg/(Fe^{2+} + Mg)) and y_{Al}(Opx) in order to retrieve peak *P–T* conditions. The interpreted peak assemblage of garnet + orthopyroxene + biotite + melt is stable over a wide P–T range (>7.5 kbar and >860 ℃). The measured highest y_{Al} (0.18–0.19) and X_{Mg} (0.775−0.780) in orthopyroxene intersect at 12−13 kbar and 1070−1130 ℃, which is interpreted as the peak *P–T* conditions.

The peak minerals usually show breakdown to intergrowths of orthopyroxene$_2$ + cordierite ± biotite ± plagioclase ± spinel or sapphirine + cordierite at the post−peak stage. As shown in the enlarged P–T diagram (P = 5.0–9.0 kbar and T = 800–1000 ℃) (Fig. 13b), these assemblages occupy a narrow field, constraining the *P–T* conditions to 6.5–7.0 kbar and 910–950 ℃ (outlined by purple bold lines). Plagioclase from the orthopyroxene–cordierite–bearing intergrowths has a typical X_{An} of 0.80–0.81, consistent with the prediction by the modeling. The inferred final assemblage is featured by later growth of sapphirine, biotite and plagioclase, which is predicted to be stable at a narrow pressure range of 6.5–6.8 kbar, with temperatures varying from 825 to 900 ℃. This field is bounded by the fluid–absent solidus, rutile–in, garnet– and ilmenite–out curves. The

510 measured X_{Mg} in biotite (~0.81) and X_{An} in plagioclase (0.51–0.58) are consistent with the P–T
511 field, further constraining the cooling path through *P–T* conditions of 6.5–7.0 kbar and 830–870 ℃
512 (outlined by black bold lines).
513
514 **Tracking the pre–peak melting process with melt–reintegration**
515 Phase equilibria modeling suggests that the solidus is located between 800 and 870 °C (at 3–7 kbar)
516 and the rock produces <15 vol.% melt at the peak stage, which is much lower than the expected
517 values for metapelites. In addition, biotite is predicted to be stable at >1100 °C (Fig. 13a). All these
518 observations are in agreement with the strongly residual character of the bulk rock composition
519 (SiO_2 = 44 wt.%). Thus, this composition obtained from XRF analysis is only appropriate for
520 modeling the peak and post–peak metamorphic evolutions (White et al., 2004; Liu et al., 2020).
521 Here we explore the potential effects of melt loss on the topology during pre–peak evolution by
522 reintegrating a certain amount of melts to the residual composition (Bartoli, 2017, 2019). The
523 simplified chemical systems with respect to natural occurrences (Bartoli & Carvalho, 2021) and the
524 limitations of solution models (White et al., 2011) make it impossible to precisely predict the
525 primary melt compositions of partially melted rocks. As a consequence, NIs are used as proxy of the
526 pristine melts that was present in the system (e.g. Bartoli, 2019). This single–step melt–
527 reintegration may be only suitable to reconstruct the probable bulk rock compositions (BRC) at or
528 near *UHT* conditions as the rock may have undergone several episodes of melt loss (e.g. Bartoli,
529 2017; White et al., 2014) and the compositions of NIs cannot represent the melt compositions
530 generated at low temperatures.
531 The presence of trapped rutile grains within NIs are confirmed by Raman analyses (Fig. 5g),
532 but not observed in the matrix or predicted by the phase equilibria modeling (Fig. 13). As shown in
533 Figure 14a, rutile is expected to appear at >950 ℃ if >20 mol.% melts are reintegrated back into the
534 rock. This is consistent with their presence as trapped phase within the NIs (Fig. 5g), and is strongly
535 supportive of the entrapment of rutile−bearing melt inclusions at *UHT* conditions. With 25 mol.%
536 melts reintegrated back into the BRC, the modeling predicts that most melts (~40 mol.%) were
537 produced in the temperature range of 850−950 ℃. The melt reintegration also results in a reduction
538 of the stability field of biotite, which is predicted to disappear at >950 °C (Fig. 14a). The melt
539 composition calculated at 12.5 kbar and 950 ℃ shows slightly higher Na_2O and K_2O contents

(Table 3). This divergence between NIs and the calculated melts was also documented in other case studies, and was ascribed to the lack of equilibrium with the residuum or diffusion in the melts, and alternatively, the imperfections of forward phase equilibria modeling (Bartoli & Carvalho, 2021).

The *P*−*T* pseudosection reconstructed with a reintegration of 25 mol.% melts into the BRC is shown in Figure 14b. The most evident changes are expansions of the stability fields of K−feldspar and rutile, which were predicted to be stable during prograde melting. Despite the fact that kyanite/sillimanite is absent in the investigated rocks, kyanite pseudomorphs (Tong & Wilson, 2006) and kyanite relics replaced by sapphirine + quartz (Harley, 2021) have been identified in rocks from the same region, suggesting that the rocks may have been in the kyanite stability field. The quartz−, kyanite−in and plagioclase−out curves suggest that the rocks underwent a nearly isobaric heating from M0 to M1 stage (shown by dashed lines in Figure 13a). Accordingly, the Mather *UHT* granulites may have experienced a clockwise *P–T* path with peak conditions of 12−13 kbar and 1070−1130 °C, followed by decompression and cooling to 6.5–7.0 kbar and 910–950 °C, and finally isobaric cooling (IBC) to solidus conditions (P = 6.5–7.0 kbar; T = 830–870 °C).

DISCUSSIONS

P–T conditions of melt entrapment and anatectic regime

In East Antarctica, NIs in high–grade metamorphic rocks have been reported from the Lützow–Holm Complex (Spr–bearing *UHT* metapelitic granulites; Carvalho et al., 2023a), the Dronning Maud Land (ultramafic granulites; Ferrero et al., 2018), the Northern Victoria Land (metagreywackes; Ferri et al., 2020), and the Sør Rondane Mountains (East Antarctica) (Sil–Grt–Bt gneiss; Higashino & Kawakami, 2022). The present study expands the existing database to include the melts produced by *UHT* metamorphism of the Mg–rich and Sil–absent metapelitic rocks from the Rauer Islands.

The presence of kokchetavite and kumdykolite is confirmed by Raman analyses (Fig. 5g). Kokchetavite has been found within multiphase inclusions in high to ultrahigh pressure (*HP–UHP*) rocks, which was considered to crystalize from K–rich melts and may exist as a metastable phase (e.g. Borghini et al., 2018, 2023; Ferrero et al., 2016; Gao & Liu, 2018; Hwang et al., 2004, 2013). Kumdykolite was not only present as inclusions within *HP–UHP* rocks (e.g. Borghini et al., 2018, 2023; Ferrero et al., 2016; Gao & Liu, 2018; Hwang et al., 2009; Kotková et al., 2014), but also

found in chondrites (Németh et al., 2013). However, Ferrero et al. (2016) concluded that high pressure is not required for the formation of kumdykolite and kokchetavite, and their presence is thus not an indicator of *UHP* conditions. More recently, NIs from granulites have also been reported to preserve kokchetavite and/or kumdykolite as daughter phases (Carvalho et al., 2019; Ferrero & Angel, 2018; Gianola et al., 2021). Therefore, both kokchetavite and kumdykolite may have crystalized from *HT* to *UHT* melts, and cannot be used to infer the *P–T* entrapment conditions. According to Ferrero et al. (2016), the presence of feldspar polymorphs indicates that the melt compositions (in terms of major elements and volatiles) are mostly preserved.

Melting during heating is predicted by phase equilibria modeling (Figs. 13, 14). Rutile is present within NIs as an accidentally trapped phase (Fig. 5g). However, it is not observed in the matrix of the rocks. This suggests that rutile existed in the pre−peak stage and became metastable as a consequence of melt extraction and loss. After an integration of ~25% melts into the granulitic restite, phase equilibria modeling predicts that rutile appears when temperature exceeds 950 ℃ at 12.5 kbar (Fig. 14), highly in agreement with the remelting experimental constraints given by NIs at 12.5 kbar. Furthermore, some NIs occur near to high−Al orthopyroxene inclusions (Al_2O_3 = 8.85−9.04 wt.%) within garnets (Fig. 3a). These are strong evidence that at least some NIs investigated in this study were trapped at *UHT* conditions. Although the rocks studied here have undergone peak temperatures of 1070−1130 ℃, the melts may be produced at or near *UHT* conditions (850−950 ℃).

The H_2O contents of NIs show variable values ranging from 1.49 to 4.24 wt.% (Table 3), suggestive of heterogeneous distributions of water (Bartoli et al., 2014) or existences of C–bearing phases in some NIs (e.g. Carvalho et al., 2019; Ferri et al., 2020; Gianola et al., 2021). Estimation of H_2O by difference of EMPA totals from 100% usually overestimates the H_2O contents of NIs (e.g. Cesare et al., 2015), and specific reasons for this inconsistency still need further investigations. As shown in Figures 9 and 10, the highly silicic, peraluminous and potassic to ultrapotassic NIs have also been found in peritectic garnets from the Kerala Khondalite Belt (Cesare et al., 2009; Ferrero et al., 2012), the Gruf Complex (Gianola et al., 2021) and the Lützow–Holm Complex (Carvalho et al., 2023a). Moreover, K–rich melts have also been experimentally derived from pelitic starting materials under *UHT* conditions (e.g. Droop et al., 2003; Patiño–Douce & Johnston, 1991). Ti and Fe^{3+} are expected to stabilize biotite to expand the Bt–dehydration melting to occur at higher

temperatures (e.g. White et al., 2014), which likely accounts for the enrichments of K_2O in *HT* to *UHT* melts (Gianola et al., 2021). However, it is also evident that melt compositions of *HT–UHT* granulites from the Ivrea Zone plot away from the K−apex of the triangle (Fig. 10), with low K_2O contents of ~2.0 wt.% (Carvalho et al., 2019). The authors argued that the low–K melts may be produced at *P–T* conditions approaching the Bt–out curves (Carvalho et al., 2019). Alternatively, participation of plagioclase in the prograde melting reactions may also be responsible for the relatively higher CaO/NaO concentrations in that study. The potassic nature of melts, coupled with phase equilibria modeling (Fig. 14), supports that the melts were produced by Bt–dehydration melting of pelites under *HT* to *UHT* conditions (850−950 °C).

Our data show that the melts are enriched in Li, Cs, Rb, Ta, Sm, Nd, Zr, U and Pb and depleted in Ce, Th, Ba, Sr and Nb relative to the granulitic restite (Table 4; Fig. 11). Dissolution of zircon or monazite during high temperature melting (Kelsey & Powell, 2011) may contribute to the U, Pb and Zr enrichments in anatectic melts. NIs in this study are depleted in Ce (<12.8 ppm) and Th (<3.8 ppm), which may be ascribed to the shielding of some monazites by porphyroblastic phases (Huang et al., 2021) or disequilibrium melting (Watt & Harley, 1993). It suggests that the melts are likely undersaturated with respect to monazite. Besides, the melts show mild depletion of Ba compared with the restite. K−feldspar is the most important repository of Ba in the rocks and it was still stable during melting, which might reserve appreciable amounts of Ba (Zeng et al., 2005).

The investigated melts contain higher Rb contents than the melts produced through Ms−dehydration melting (Acosta−Vigil et al., 2010, 2012; Bartoli et al., 2019), consistent with melts yielded by Bt−dehydration melting because biotite is the major reservoir of Rb (e.g. Acosta−Vigil et al., 2010; Wolf et al., 2019). They also show higher Rb contents relative to the matrix glasses from El Hoyazo (Fig. 11), which were considered to be yielded at the onset of biotite−dehydration melting (Acosta−Vigil et al., 2010). Moreover, Sr contents are usually low in micas but abundant in plagioclase (Weinberg & Hasalová, 2015), and plagioclase was not involved in the incongruent melting in this study. Thus, higher Rb/Sr ratios of the investigated NIs can be attributed to Bt−dehydration melting in the absence of plagioclase. On the other hand, although Zeng et al. (2005) previously pointed out that that Ms/Bt−dehydration melting and dissolution of apatite will produce melts with high Sm/Nd values, the mechanisms that caused elevated Sm/Nd ratios in the melts are still vague. Assuming no isotopic fractionations of Nd and Sr, enrichments of

Sm and Rb in anatectic melts are expected to result in higher $^{143}Nd/^{144}Nd$ and $^{87}Sr/^{86}Sr$ values in melts than the granulitic restite after enough long time.

Physical properties of the hottest crustal melts

The chemical data of NIs allow to peer into physical properties of the melts and therefore, may provide insights into rheology and mobility of the hottest granitic melts and their potential effects on orogenic evolution. Assuming conditions of P = 12 kbar and T = 950 °C, the average compositions of re–homogenized melt inclusions are considered to have densities of 2.47 ± 0.07 g/cm^3, calculated with program DensityX (Iacovino & Till, 2019). These values are slightly higher than previously estimated densities for hydrous granitic melts (~2.20 g/cm^3; Clemens & Vielzeuf, 1987), but lower than the average density for granites (~2.70 g/cm^3; Artemieva et al., 2017).

Viscosity of melts may be affected by several potential factors, such as fluid contents (Holtz et al., 2001; Scaillet et al., 1996) and melt compositions (Giordano et al., 2008). At 950 °C, applications of the equations of Giordano et al. (2008) and Scaillet et al. (1996) yield melt viscosities of $10^{4.1}$–$10^{6.1}$ Pa·s and $10^{4.0}$–$10^{5.2}$ for the investigated melts, respectively. When considering the average melt compositions, these methods produce results of $10^{4.9\pm1.2}$ and $10^{4.6\pm0.8}$ Pa·s. As the estimated H_2O contents for the melts based on difference of EMPA totals from 100% usually slightly higher than their real values due to the possible presence of CO_2 (e.g. Cesare et al., 2015), the calculated viscosities may represent the minimum values. Viscosities for the investigated melts are roughly in agreement with the calculation results for melt inclusions within *UHT* granulites from the Gruf Complex ($10^{4.1}$–$10^{4.8}$ Pa·s; Gianola et al., 2021). These values also overlap the estimates of granitic melts that were experimentally derived at 5–8 kbar and 700–950 °C ($10^{4.3}$–$10^{5.4}$ Pa·s) (Hess & Dingwell., 1996; Scaillet et al., 1996). However, melts formed at low temperature (~700 °C) showed higher viscosities (~$10^{6.0}$ Pa·s) (Bartoli et al., 2013b), and therefore less mobile and result in slower rates of melt segregation and ascent (Bartoli et al., 2013b; Brown, 2013; Holtz et al., 2001). Clemens et al. (2020) concluded that melting at high temperatures (mostly >850 °C) under fluid−deficient or –absent conditions are usually highly mobile, and therefore, the low viscosity melts may facilitate melt extraction, and consequently crustal differentiation and redistribution of heat−producing elements (such as K, Th and U) (Gianola et al., 2021).

660 The melts are enriched in heat producing elements such as K and U. Despite that the melts are
661 depleted in Th, the heat production rate of Th (0.072 μW/m^3) is much lower than that of U (0.265
662 μW/m^3) (Bea, 2012). The capacity for heat production of the hot melts was determined with the
663 following equation (Rybach, 1988):
664 $H = \rho \times (0.0952 \times C_U + 0.0348 \times C_K + 0.0256 \times C_{Th})$
665 Where H is heat production in μW/m^3, ρ is density in g/cm^3, and C_U, C_K, and C_{Th} are
666 concentrations of radioactive isotopes of U, K, and Th in ppm, wt.% and ppm, respectively.
667 As calculated above, the density of melts is estimated as 2.47 ± 0.07 g/cm^3. Calculated heat
668 production value for the average melt composition is ~2.3 μW/m^3. However, the obtained K, U and
669 Th contents of melts cannot represent their real concentrations during the thermal event because of
670 long–standing decay of the parental elements. Accordingly, heat production of average melt
671 compositions was back-calculated to ~530 Ma based on appropriate decay equations for ^{238}U, ^{235}U,
672 ^{232}Th and ^{40}K. The resultant average value is ~2.8 μW/m^3, which is higher compared with bulk heat
673 production in granitic rocks of all ages (~2.0 μW/m^3; Artemieva et al., 2017).
674 Granitic melts investigated in this study are particularly rich in heat–producing elements (such
675 as K and U), and show densities of 2.47 ± 0.07 g/cm^3 and viscosities of $10^{4.9\pm1.2}$ Pa•s. Such melts
676 are mobile and prone to be extracted from the source, and as a consequence, might be responsible
677 for the formation of large granitic intrusions. Stagnation and flow of such melts in the deep crust
678 provides a potential source at the base of the crust to heat the orogenic hinterlands through
679 radioactive decay of heat producing elements (Clark et al., 2011; Gianola et al., 2021), and may
680 have a great influence on the thermal structure of the continental crust.
681
682 **Secondary fluid infiltration and its implications for the timing of *UHT* metamorphism: open**
683 **questions**
684 Fluid infiltration is a well−documented phenomenon in the Rauer Islands. For example, Harley
685 (1998b) has suggested the growth of cordierites in Grt–Sil–Qz gneiss was linked with the ingress of
686 CO_2–rich fluid ($X_{CO2} > 0.8$) based on secondary ion mass spectrometry analyses of H_2O and CO_2 in
687 the secondary cordierite. On the contrary, coarser cordierites adjacent to leucosomes show lower
688 X_{CO2} values of 0.05. Such features indicate that the fluid regime in this region has changed
689 markedly as a consequence of ambient C–O–H fluid ingress. As zircon U–Pb systematics of the

layered mafic complex and intrusive tonalites from the nearby Scherbinina Island show clear resetting at ~520 Ma, the fluid ingress was considered to have occurred at 530–510 Ma (Harley et al., 1998; Harley & Kelly, 2007). On the other hand, Liu et al. (2021) reported that hornblende and clinopyroxene in mafic granulites from the Filla Island were partially replaced by actinolite, which was also ascribed by the authors to strong fluid activities during the Cambrian reworking. In this study, we report on the occurrence of multiphase fluid inclusions (i.e. magnesite, pyrophyllite, corundum and CO_2) within orthopyroxene and garnet (Fig. 7), which are considered to be secondary in origin. Such stepdaughter phases were previously recognized in garnet−hosted primary FIs (e.g. Carvalho et al., 2020, 2023b; Gianola et al., 2021; Tacchetto et al., 2019). Here, we confirm that the secondary C−O−H fluid along the healed fractures of garnet and orthopyroxene at high temperatures could not survive neither, and has reacted with its hosts to produce CO_2 and OH−bearing phases during cooling (possibly at 400−600 °C; Carvalho et al., 2020). Pure CO_2 inclusions within garnets are also present, which might represent the fluid that infiltrated into the rocks at a very late stage.

In regard of the origin of the fluid, several potential sources can be considered. Harley et al. (1998) speculated that the infiltration of CO_2–rich fluid might have occurred during the decompression as a consequence of emplacements of granitic pegmatites in the Cambrian (Kinny et al., 1993). Additionally, coeval graphite–bearing sediments (e.g. Harley & Fitzsimons, 1991) and forsterite marbles (e.g. Buick et al., 1994; Harley, 1998b) have been reported in the Rauer Islands, and their decarbonation may also be external sources for the fluid. Collectively, an external source for the C–O–H fluid is favored in this study. Fluid infiltration not only lead to possible transfer of fluid–related elements (e.g. Liu et al., 2018), but also caused partial to complete resetting of U–Th–Pb systems in zircon and monazite (e.g. Das et al., 2021; Harley et al., 1998; Harley & Kelly, 2007; Taylor et al., 2014).

As addressed on the section of geological setting, the timing of the *UHT* metamorphism is still a matter of debate. Constraints on its timing are critical to understanding the tectono–thermal evolution of the Rauer Islands, and even the whole Prydz Belt. Some works proposed that the Prydz Belt represents an early Neoproterozoic (~1000 Ma) metamorphic complex that was reworked by a Pan–African (~530 Ma) thermal event (e.g. Liu et al., 2009, 2014; Tong et al., 2014b, 2019; Wang et al., 2008), and the *UHT* metamorphism in the Rauer Islands occurred at ~1000 Ma (Tong &

Wilson, 2006; Wang et al., 2007). This point of view has not been accepted by other researchers, who argued that this episode of *UHT* metamorphism may have taken place in the late Neoproterozoic to Cambrian (e.g. Clark et al., 2019; Kelsey et al., 2003, 2007) or prior to ~590 Ma (Hokada et al., 2016; Harley et al., 2009). Our dating results for zircon mantles show variable dates ranging from 1050 to 607 Ma (Fig. 12e; Table 5). Previous U−Pb dating on Spr−bearing *UHT* granulites from the same locality also showed similar age spreads from 1000 Ma to 500 Ma (Hokada et al., 2016; Wang et al., 2007). Such scattered ages were previously interpreted as mixed ages, detrital ages, or ascribed to variable effects of the Pan–African thermal event on pre–existing zircons (Hokada et al., 2016; Spreitzer et al., 2021; Wang et al., 2022). Although we cannot preclude the possibility of melt–mediated–coupled dissolution–precipitation of zircons in the Cambrian (Wang et al., 2022), findings of secondary FIs in peritectic phases (such as garnet, orthopyroxene) and zircons in this study seem to support that the broad range of isotopic dates may be partially caused by extensive C–O–H fluid infiltration at high temperature conditions (>600 ℃). Till now, all the U–Th–Pb dating on monazite pointed to metamorphic ages of 580–510 Ma (Clark et al., 2018; Hokada et al., 2016; Kelsey et al., 2003, 2007; Liu et al., 2021). Here, we prefer the interpretation that U–Th–Pb clock of monazites has been completely reset as they were more vulnerable to fluid ingress compared with zircons (e.g. Das et al., 2021; Taylor et al., 2014).

Additionally, garnet inclusions within zircon mantles from mafic granulites in the Archean crustal domain indicate that the post–peak decompression and cooling probably occurred at 540–471 Ma (our own unpublished data), roughly consistent with the dates documented by zircon rims in this study (569–472 Ma). If it is the case, the peak metamorphism took place at least prior to ~570 Ma. Hokada et al. (2016) reported the microstructure and CL image of an orthopyroxene−hosted zircon inclusion from the same outcrop, and it documents ages of 2502 Ma in the core and 1254−1148 Ma in the rim. This suggests that this type of zircons has not been affected by the Pan−African thermal event likely due to the shielding effect of orthopyroxene. Five dark–CL mantles show $^{206}Pb/^{238}U$ dates of 1050–940 Ma (Table 5), which however, are slightly discordant (Fig. 12f). Up to now, the most concordant ages for the Spr–bearing *UHT* granulites from the Mather Peninsula were obtained by Wang et al. (2007), which yielded a weighted mean $^{207}Pb/^{206}Pb$ age of 995 ± 15 Ma. Nonetheless, their dating results also showed some discordance from 1000 Ma toward 530 Ma (Wang et al., 2007). The present study highlights that C–O–H fluid

infiltration and alternatively, melt–mediated–coupled dissolution–precipitation during the Pan–African reworking, have contributed to the partial resetting of U–Th–Pb systems in zircons. Collectively, the *P–T* framework (Fig. 15) might be linked with two separated thermal events that happened at ~1000 Ma and ~530 Ma, respectively. We propose that the *UHT* metamorphism and relevant melting most likely occurred prior to ~570 Ma (Harley et al., 2009; Hokada et al., 2016), while the post–peak decompression and the final cooling happened at 570–470 Ma (Fig. 15). However, it is still far from precisely determining the timing of *UHT* metamorphism in this region, which requires further investigations.

CONCLUSIONS

Phase equilibria modeling suggests that the Spr–bearing *UHT* granulites from the Mather Peninsula (East Antarctica) have undergone a clockwise *P–T* path, with peak conditions of 12−13 kbar and 1070−1130 ℃. Melt and fluid inclusions are characterized in this study. Coupled with chronological dating results, the main conclusions drawn are described below:

1) Abundant NIs are preserved within garnet, which are usually 5–15 μm in diameter and display typically negative crystal shapes. NIs have crystallized into polycrystalline aggregates, comprising daughter phases of quartz, biotite, kokchetavite, kumdykolite and an unknown phase (phase “430”). Petrographic observations and mineral chemistry suggest that the melts were at least partially yielded at *UHT* conditions. The NIs were perfectly re−homogenized with a piston cylinder apparatus at ~12 kbar and ~950 ℃, and show SiO_2–rich, strongly peraluminous and potassic to ultrapotassic composition.

2) Compared with the granulitic restite, the NIs are enriched in Li, Cs, Rb, Ta, Sm, Nd, Zr, U and Pb, and depleted in Ce, Th, Ba, Sr and Nb. Melting mechanisms and dissolution of accessory minerals played a key role in the partitioning of elements between anatectic melts and their granulitic counterparts. High Rb/Sr and Sm/Nd ratios for the melts, coupled with phase equilibria modeling, suggest that the melts were formed by fluid−absent Bt−dehydration melting. These *UHT* crustal melts have densities of 2.47 ± 0.07 g/cm^3, viscosities of $10^{4.9\pm1.2}$ Pa·s and high heat production values of ~2.8 μW/m^3. As a consequence, these melts are expected to be mobile and may have played an important role in redistribution of heat−producing elements (such as K and U).

3) Secondary FIs are distributed along healed fractures of the peritectic phases (such as garnet

and orthopyroxene), typically comprising magnesite, corundum, pyrophyllite and residual CO_2 (ρ_{CO2} = 0.2–1.0 g/cm^3). They are interpreted as stepdaughter phases due to interaction between C−O−H fluid and their hosts during post−peak metamorphic evolutions. Pure CO_2 inclusions with a density of ~0.8 are also present, representing the fluid that infiltrated the rock at a very late stage. Ingress of the C–O–H fluid under high temperatures probably resulted in mobility and loss of Pb in zircons, and was likely responsible for the large date span of zircon mantles from 1050 to 607 Ma. Another possible reason is melt–mediated–coupled dissolution–precipitation during the Pan–African reworking. Therefore, the retrieved *P–T* path might be linked with two separated thermal events happened at ~1000 and ~530 Ma, respectively. Although metamorphic timing for the UHT metamorphism is still debated, we conclude that the peak metamorphism occurred prior to ~570 Ma.

ACKNOWLEDGEMENTS

This research was financially supported by the NSFC projects (42102043, 41972050) and the China Postdoctoral Science Foundation (2020M683535). This study also benefitted from funding of the Programma Nazionale di Ricerca in Antartide 2018 (PNRA18_00103 to B.B. Carvalho) and Padua University (BART_SID19_01 to O. Bartoli; WelcomeKit to B.B. Carvalho). We thank the leaders and members of the 33rd and 39th Chinese National Antarctic Research Expedition (CHINARE) for the logistic support during the Antarctic field work. We are especially grateful to Prof. J. Liu for his involvement in the field work. Dr. W.Q. Yang and Dr. C. Li are thanked for his help in the electronic microprobe analyses for mineral compositions. Dr. Y.G. Feng from Chang'an University is acknowledged for his help in the Raman analyses. We are deeply indebted to Dr. J.Y. Pan, J.M. Cui and J.Y. Ding from Nanjing University for their kind help during the LA−ICP−MS analyses for trace element of melt inclusions. We are grateful to Prof. Georg Zellmer (editor−in−chief) and Sherlock Sarah (editor) for their editorial work, and Alessia Borghini, Tetsuo Kawakami and Jon Pownall for their constructive comments that greatly improved the paper.

REFERENCES

Acosta−Vigil, A., Buick, I., Hermann, J., Cesare, B., Rubatto, D., London, D. & Morgan VI, G. B. (2010). Mechanisms of crustal anatexis: a geochemical study of partially melted metapelitic enclaves and host dacite, SE Spain. Journal of Petrology **51**, 785–821.

Acosta−Vigil, A., London, D. & Morgan, G. B. (2012). Chemical diffusion of major components in granitic liquids: Implications for the rates of homogenization of crustal melts. Lithos **153**, 308–323.

Artemieva, I. M., Thybo, H., Jakobsen, K., Sørensen, N. K. & Nielsen, L. S. K. (2017). Heat production in granitic rocks: Global analysis based on a new data compilation GRANITE2017. Earth–Science Reviews **172**, 1–26

Bartoli, O., Cesare, B., Poli, S., Acosta–Vigil, A., Esposito, R., Turina, A., Bodnar, R. J., Angel, R. J. & Hunter, J. (2013a). Nanogranite inclusions in migmatitic garnet: behavior during piston–cylinder remelting experiments. Geofluids **13**, 405–420.

Bartoli, O., Cesare, B., Poli, S., Bodnar, R. J., Acosta–Vigil, A., Frezzotti, M. L. & Meli, S. (2013b). Recovering the composition of melt and the fluid regime at the onset of crustal anatexis and S–type granite formation. Geology **41**, 115–118.

Bartoli, O., Cesare, B., Remusat, L., Acosta–Vigil, A. & Poli, S. (2014). The H_2O content of granite embryos. Earth and Planetary Science Letters **395**, 281–290.

Bartoli, O., Acosta–Vigil, A., Ferrero, S. & Cesare, B. (2016). Granitoid magmas preserved as melt inclusions in high–grade metamorphic rock. American Mineralogist **101**, 1543–1559.

Bartoli, O. (2017). Phase equilibria modelling of residual migmatites and granulites: An evaluation of the melt–reintegration approach. Journal of Metamorphic Geology **35**, 919–942.

Bartoli, O. (2019). Reintegrating nanogranitoid inclusion composition to reconstruct the prograde history of melt–depleted rocks. Geoscience Frontiers **10**, 517–525.

Bartoli, O., Acosta-Vigil, A., Cesare, B., Remusat, L., Gonzalez-Cano, A., Wälle, M., Tajčmanová, L. & Langone, A. (2019). Geochemistry of Eocene-Early Oligocene low-temperature crustal melts from Greater Himalayan Sequence (Nepal): a nanogranitoid perspective. Contributions to Mineralogy and Petrology **174**, 82.

Bartoli, O. & Carvalho, B. B. (2021). Anatectic granites in their source region: A comparison between experiments, thermodynamic modelling and nanogranitoids. Lithos 402–403, 106046.

841 Bea, F. (2012). The sources of energy for crustal melting and the geochemistry of heat producing
842 elements. Lithos **153**, 278–291.
843 Berkesi, M., Hidas, K., Guzmics, T., Dubessy, J., Bodnar, R. J., Szabó, C., Vajna, B. & Tsunogae, T.
844 (2009). Detection of small amounts of H_2O in CO_2–rich fluid inclusions using Raman
845 spectroscopy. Journal of Raman Spectroscopy **40**, 1461–1463.
846 Borghini, A., Ferrero, S., Wunder, B., Laurent, O., O'Brien, P. J. & Ziemann, M. A. (2018).
847 Granitoid melt inclusions in orogenic peridotite and the origin of garnet clinopyroxenite.
848 Geology **46**, 1007–1010.
849 Borghini, A., Nicoli, G., Ferrero, S., O'Brien, P. J., Laurent, O., Remusat, L., Borghini, G. & Milani,
850 S. (2023). The role of continental subduction in mantle metasomatism and carbon recycling
851 revealed by melt inclusions in UHP eclogites. Science Advances **9**, eabp9482.
852 Brown, M. (2007). Metamorphic conditions in orogenic belts: a record of secular change.
853 International Geology Review **49**, 193–234.
854 Brown, M. (2013). Granite: From genesis to emplacement. GSA Bulletin **125**, 1079–1113.
855 Cavalcante, G. C. G., Viegas, G., Archanjo, C. J. & da Silva, M. E. (2016). The influence of partial
856 melting and melt migration on the rheology of the continental crust. Journal of Geodynamics
857 **101**, 186–199.
858 Carvalho, B. B., Bartoli, O., Ferri, F., Cesare, B., Ferrero, F., Remusat, L., Capizzi, L. & Poli, S.
859 (2019). Anatexis and fluid regime of the deep continental crust: new clues from melt and fluid
860 inclusions in metapelitic migmatites from Ivrea Zone (NW Italy). Journal of Metamorphic
861 Geology **37**, 951–975.
862 Carvalho, B. B., Bartoli, O., Cesare, B., Tacchetto, T., Gianola, O., Ferri, F., Aradi, L. E. & Szabó, C.
863 (2020). Primary CO_2–bearing fluid inclusions in granulitic garnet usually do not survive. Earth
864 and Planetary Science Letters **536**, 116170.
865 Carvalho, B.B., Bartoli, O., Cesare, B., Satish–Kumar, M., Petrelli, M., Kawakami, T., Hokada, T.
866 & Gilio, M. (2023a). Revealing the link between A–type granites and hottest melts from
867 residual metasedimentary crust. Geology. Doi.org/10.1130/G51097.1
868 Carvalho, B. B., Bartoli, O. & Cesare, C. (2023b). C–O–H fluid–melt–rock interaction in graphitic
869 granulites and problems of quantifying carbon budget in the lower continental crust. Chemical
870 Geology **631**, 121503.
871 Cenki, B., Kriegsman, L. M. & Braun, I. (2002). Melt−producing and melt−consuming reactions in

anatectic granulites: P–T evolution of the Achankovil cordierite gneisses, South India. Journal of Metamorphic Geology **20**, 543–561.

Cesare, B., Satish−Kumar, M., Cruciani, G., Pocker, S. & Nodari, L. (2008). Mineral chemistry of Ti–rich biotite from pegmatite and metapelitic granulites of the Kerala Khondalite Belt (Southeast India): petrology and further insight into titanium substitutions. American Mineralogist **93**, 327–338.

Cesare, B., Ferrero, S., Salvioli–Mariani, E., Pedron, D. & Cavallo, A. (2009). Nanogranite and glassy inclusions: the anatectic melt in migmatites and granulites. Geology **37**, 627–630.

Cesare, B., Acosta–Vigil, A., Bartoli, O. & Ferrero, S. (2015). What can we learn from melt inclusions in migmatites and granulites? Lithos **239**, 186–216.

Chappell, B. W. (1999). Aluminium saturation in I− and S−type granites and the characterization of fractionated haplogranites. Lithos **46**, 535–551.

Chen, L. Y., Liu, X. C., Wang, W–(RZ). & Liu, J. (2023). Ultrahigh–Temperature Mafic Granulites in the Rauer Group, East Antarctica: Evidence from Conventional Thermobarometry, Phase Equilibria Modeling, and Rare Earth Element Thermometry. Journal of Petrology **64**, 1–28.

Clark, C., Fitzsimons, I. C. W., Healy, D. & Harley, S. L. (2011). How does the continental crust get really hot? Elements **7**, 235–240.

Clark, C., Taylor, R. J. M., Johnson, T. E., Harley, S. L., Fitzsimons, I. C. W. & Oliver, L. (2019). Testing the fidelity of thermometers at ultrahigh temperatures. Journal of Metamorphic Geology **37**, 917–934.

Clemens, J. D. & Vielzeuf, D. (1987). Constraints on melting and magma production in the crust. Earth and Planetary Science Letters **86**, 287−306.

Clemens, J. D., Stevens, G. & Bryan, S. E. (2020). Conditions during the formation of granitic magmas by crustal melting–Hot or cold; drenched, damp or dry? Earth–Science Reviews **200**, 102982.

Connolly, J. A. D. (2005). Computation of phase equilibria by linear programming: a tool for geodynamic modeling and its application to subduction zone decarbonation. Earth and Planetary Science Letters **236**, 524–541.

Das, K., Bose, S., Torimoto, J., Hayasaka, Y. & Dunkley, D. (2021). Tracking C–O–H fluid–rock interactions in reworked UHT granulite: Tectonic evolution from ca. 990 Ma to ca. 500 Ma in orogenic interior of Eastern Ghats Belt, India. Lithos **398–399**, 106287.

Diener, J. F. A. & Fagereng, Å. (2014). The influence of melting and melt drainage on crustal rheology during orogenesis. Journal of Geophysical Research.: Solid Earth 119, 6193–6210.

Dirks, P. H. G. M. & Wilson, C. J. L. (1995). Crustal evolution of the east Antarctic mobile belt in Prydz Bay: continental collision at 500Ma? Precambrian Research **75**, 189–207.

Droop, G. T. R., Clemens, J. D. & Dalrymple, D. J. (2003). Processes and conditions during contact anatexis, melt escape and restite formation: The Huntly Gabbro Complex, NE Scotland. Journal of Petrology **44**, 995–1029.

Ewing, T. A., Hermann, J. & Rubatto, D. (2013). The robustness of the Zr–in–rutile and Ti–in–zircon thermometers during high-temperature metamorphism (Ivrea-Verbano Zone, northern Italy). Contributions to Mineralogy and Petrology **165**, 757–779.

Ferrero, S., Bartoli, O., Cesare, B., Salvioli–Mariani, E., Acosta–Vigil, A., Cavallo, A., Groppo, C. & Battiston, S. (2012). Microstructures of melt inclusions in anatectic metasedimentary rocks. Journal of Metamorphic Geology **30**, 303–322.

Ferrero, S., Ziemann, M. A., Angel, R. J., O'Brien, P. J. & Wunder, B. (2016). Kumdykolite, kokchetavite, and cristobalite crystallized in nanogranites from felsic granulites, Orlica-Snieznik Dome (Bohemian Massif): not an evidence for ultrahigh-pressure conditions. Contributions to Mineralogy and Petrology **171**, 3.

Ferrero, S. & Angel, R. J. (2018). Micropetrology: Are Inclusions Grains of Truth? Journal of Petrology **59**, 1671–1700.

Ferrero, S., Godard, G., Palmeri, R., Wunder, B. & Cesare, B. (2018). Partial melting of ultramafic granulites from Dronning Maud Land, Antarctica: Constraints from melt inclusions and thermodynamic modelling. American Mineralogist **103**, 610–622.

Ferrero, S., Wannhoff, I., Laurent, O., Yakymchuk, C., Darling, C., Wunder, B., Borghini, A. & O'Brien, P. J. (2021a). Embryos of TTGs in Gore Mountain garnet megacrysts from water−fluxed melting of the lower crust. Earth and Planetary Science Letters **569**, 117058.

Ferrero, S., Ague, J. J., O'Brien, P. J., Wunder, B., Remusat, L., Ziemann, A. & Axler, J. (2021b). High pressure, halogen−bearing melt preserved in ultra−high temperature felsic granulites of the Central Maine Terrane, Connecticut (US). American Mineralogist **106**, 1224−1236.

Ferri, F., Cesare, B., Bartoli, O., Ferrero, S., Palmeri, R., Remusat, L. & Poli, S. (2020). Melt inclusions at MT. Edixon (Antarctica): Chemistry, petrology and implications for the evolution of the Lanterman range. Lithos **374–375**, 105685.

Fitzsimons, I. C. W. (2003). Proterozoic basement provinces of southern and southwestern Australia, and their correlation with Antarctica. Geological Society, London, Special Publications **206**, 93–130.

Frezzotti, M. L., Tecce, F. & Casagli, A. (2012). A. Raman spectroscopy for fluid inclusion analysis. Journal of Geochememical Exploration **112**, 1–20.

Frost, B. R. & Frost, C. D. (2008). A geochemical classification for feldspathic igneous rocks. Journal of Petrology **49**, 1955–1969.

Galli, A., Le Bayon, B., Schmidt, M. W., Burg, J. −P., Reusser, E., Sergeev, S. A. & Larionov, A. (2012). U−Pb zircon dating of the Gruf Complex: Disclosing the late Variscan granulitic lower crust of Europe stranded in the Central Alps. Contributions to Mineralogy and Petrology **163**, 353–378.

Gao, L.E., Zeng, L. & Asimow, P. D. (2017). Contrasting geochemical signatures of fluid–absent versus fluid–fluxed melting of muscovite in metasedimentary sources: The Himalayan leucogranites. Geology **45**, 39–42.

Gao, P., Zheng, Y. F. & Zhao, Z. F. (2016). Experimental melts from crustal rocks: A lithochemical constraint on granite petrogenesis. Lithos **266–267**, 133–157.

Gao, X. Y., Zheng. Y. F., Chen. Y. X. & Hu, Z. (2014). Composite carbonate and silicate multiphase solid inclusions in metamorphic garnet from ultrahigh−P eclogite in the Dabie orogen. Journal of Metamorphic Geology **32**, 961–980.

Gao, Y. J. & Liu, J. B. (2018). Research advances of melt inclusions in high–grade metamorphic rocks. Earth Science **43**, 236–246 (in Chinese with English abstract).

Gianola, O., Bartoli, O., Ferri, F., Galli, A., Ferrero, S., Capizzi, L. S., Liebske, C., Remusat, L., Poli, S. & Cesare, B. (2021). Anatectic melt inclusions in ultra high temperature granulites. Journal of Metamorphic Geology **39**, 321–342.

Giordano, D., Russell, J. K. & Dingwell, D. B. (2008). Viscosity of magmatic liquids: A model. Earth and Planetary Science Letters **271**, 123–134.

Grew, E. S., Carson, C. J., Christy, A. G., Maas, R., Yaxley, G. M., Boger, S. D. & Fanning, C. M. (2012). New constraints from U–Pb, Lu–Hf and Sm–Nd isotopic data on the timing of sedimentation and felsic magmatism in the Larsemann Hills, Prydz Bay, East Antarctica. Precambrian Research **206–207**, 87– 108.

Guillong, M., Meier, D. L., Allan, M. M., Heinrich, C. A. & Yardley, B. W. D. (2008). SILLS: a

MATLAB–based program for the reduction of laser ablation ICP–MS data of homogeneous materials and inclusions. Mineralogical Association of Canada Short Course 40, Vancouver, 328–333.

Halter, W. E., Pettke, T., Heinrich, C. A. & Rothen–Rutishauser, B. (2002). Major to trace element analysis of melt inclusions by laserablation ICP–MS: methods of quantification. Chemical Geology **183**, 63–86.

Harley, S. L. & Fitzsimons, I. C. W. (1991). Pressure–temperature evolution of metapelitic granulites in a polymetamorphic terrane: the Rauer Group, east Antarctica. Journal of Metamorphic Geology **9**, 231–243.

Harley, S. L., Snape, I. & Fitzsimons, I. C. W. (1995). Regional correlations and terrane assembly in East Prydz Bay: evidence from the Rauer Group and Vestfold Hills. Terra Antarcica 2, 49–60.

Harley, S. L. (1998a). On the occurrence and characterization of ultrahigh temperature crustal metamorphism. Geological Society, London, Special Publications **138**, 81–107.

Harley, S. L. (1998b). Ultrahigh temperature granulite metamorphism (1050 °C, 12 kbar) and decompression in garnet (Mg70)–orthopyroxene–sillimanite gneisses from the Rauer Group, East Antarctica. Journal of Metamorphic Geology **16**, 541–562.

Harley, S. L., Snape, I. & Black, L. P. (1998). The early evolution of a layered metaigneous complex in the Rauer Group, East Antarctica: evidence for a distinct Archaean terrane. Precambrian Research **89**, 175–205.

Harley, S. L. & Kelly, N. M. (2007). The impact of zircon–garnet REE distribution data on the interpretation of zircon U–Pb ages in complex high–grade terrains: An example from the Rauer Islands, East Antarctica. Chemical Geology **241**, 62–87.

Harley, S. L. (2008). Refining the P–T records of UHT crustal metamorphism. Journal of Metamorphic Geology **26**, 125–154.

Harley, S. L., Hokada, T., Montel, J. –M. & Parseval, P. (2009). Sapphirine + quartz in the Rauer Islands, Antarctica: evidence for 590 Ma UHT metamorphism and melting. In: Abstract of Granulites & Granulites Conference 2009.

Harley, S. L., Fitzsimons, I. C. W. & Zhao, Y. (2013). Antarctica and supercontinent evolution: historical perspectives, recent advances and unresolved issues. In Antarctica and Supercontinent Evolution (Harley, S.L., Fitzsimons, I.C.W. and Zhao, Y. Eds.). Geological Society of London Special Publications **383**, 1–34.

Harley, S. L. (2016). A matter of time: The importance of the duration of UHT metamorphism. Journal of Mineralogical and Petrological Sciences **111**, 50–72.

Harley, S. L. (2021). UHT metamorphism. In: Alderton, David; Elias, Scott A. (eds.) Encyclopedia of Geology, 2nd edition. United Kindom: Academic Press. Vol **2**, 522–552.

Hensen, B. J. & Zhou, B. (1997). East Gondwana amalgamation by Pan–African collision? Evidence from Prydz Bay, East Antarctica. In: Ricci, C.A. (ed.) The Antarctic Region: Geological Evolution and Processes. International Symposium on Antarctic Earth Sciences. Terra Antartica, Siena **7**, 115–119.

Hess, K. U. & Dingwell, D. B. (1996). Viscosities of hydrous leucogranitic melts: A non–Arrhenian model. American Mineralogist **81**, 1297–1300.

Higashino, F. & Kawakami, T. (2022). Ultrahigh−temperature metamorphism and melt inclusions from the Sør Rondane Mountains, East Antarctica. Journal of Mineralogical and Petrological Sciences **117**, 010.

Hiroi, Y., Hokada, T., Kato, M., Yanagi, A., Adachi, T., Osanai, Y., Mototoshi, Y. & Shiraishi, K. (2019). Felsite–nanogranite inclusions and three Al_2SiO_5 polymorphs in the same garnet in ultrahigh–temperature granulites from Rundvågshetta, Lützow–Holm Complex, East Antarctica. Journal of Mineralogical and Petrological Sciences **114**, 60–78.

Hokada, T., Harley, S. L., Dunkley, D. J., Kelly, N. M. & Yokayama, K. (2016). Peak and post–peak development of UHT metamorphism at Mather Peninsula, Rauer Islands: Zircon and monazite U–Th–Pb and REE chemistry constraints. Journal of Mineralogical and Petrological Sciences **111**, 89–103.

Holland, T. J. B. & Powell, R. (2011). An improved and extended internally consistent thermodynamic dataset for phases of petrological interest, involving a new equation of state for solids. Journal of Metamorphic Geology **29**, 333–383.

Holness, M. B., Cesare, B. & Sawyer, E. W. (2011). Melted Rocks under the Microscope: Microstructures and Their Interpretation. Elements **7**, 247–252.

Holtz, F., Johannes, W., Tamic, N. & Behrens, H. (2001). Maximum and minimum water contents of granitic melts generated in the crust: A reevaluation and implications. Lithos **56**, 1–14.

Hu, Z. C., Zhang, W., Liu, Y. S., Gao, S., Li, M., Zong, K. Q., Chen, H. H. & Hu, S. H. (2015). "Wave" signal–smoothing and mercury–removing device for laser ablation quadrupole and multiple collector ICPMS analysis: application to lead isotope analysis. Analytical Chemistry

87, 1152–1157.

Huang, G., Guo, J., Jiao, S. J. & Palin, R. (2019). What Drives the Continental Crust To Be Extremely Hot So Quickly? Journal of Geophysical Research: Solid Earth **124**, 11218–11231.

Huang, G., Guo, J. & Palin, R. (2021). Phase equilibria modeling of anatexis during ultra–high temperature metamorphism of the crust. Lithos **398–399**, 106326.

Hwang, S. L., Shen, P., Chu, H. T., Yui, T. F., Liou, J. G., Sobolev, N. V., Zhang, R. Y., Shatsky, V. S. & Zayachkovsky, A. A. (2004). Kokchetavite: a new polymorph of $KAlSi_3O_8$ from the Kokchetav UHP terrain. Contributions to Mineralogy and Petrology **148**, 380–389.

Hwang, S. L., Shen, P., Chu, H. T., Yui, T. F., Liou, J. G. & Sobolev, N. V. (2009). Kumdykolite, an orthorhombic polymorph of albite, from the Kokchetav ultrahigh–pressure massif, Kazakhstan. European Journal of Mineralogy **21**, 1325–1334.

Hwang, S. L., Yui, T. F., Chu, H. T., Shen, P., Liou, J. G. & Sobolev, N. V. (2013). Oriented kokchetavite compound rods in clinopyroxene of Kokchetav ultrahigh–pressure rocks. Journal of Asian Earth Sciences **63**, 56–69.

Iacovino, K. & Till, C. B. (2019). DensityX: A program for calculating the densities of magmatic liquids up to 1,627 °C and 30 kbar. Volcanica **2**, 1–10.

Jackson, S. E., Pearson, N. J., Griffin, W. L. & Belousova, E. A. (2004). The application of laser ablation–inductively coupled plasma–mass spectrometry to in situ U–Pb zircon geochronology. Chemical Geology **211**, 47–69.

Kawakami, T. & Motoyoshi, Y. (2004). Timing of attainment of the spinel + quartz coexistence in garnet–sillimanite leucogneiss from Skallevikshalsen, Lützow−Holm Complex, East Antarctica. Journal of Mineralogical and Petrological Sciences **99**, 311–319.

Kelsey, D. E., Powell, R., Wilson, C. J. L. & Steele, D. A. (2003). (Th+U)–Pb monazite ages from Al–Mg–rich metapelites, Rauer Group East Antarctica. Contributions to Mineralogy and Petrology **146**, 326–340.

Kelsey, D. E., Hand, M., Clark, C. & Wilson, C. J. L. (2007). On the application of in–situ monazite chemical geochronology to constraining P–T–t histories in high–temperature (>850 ◦ C) polymetamorphic granulites from Prydz Bay, east Antarctica. Journal of the Geological Society, London **164**, 667–683.

Kelsey, D. E. & Powell, R. (2011). Progress in linking accessory mineral growth and breakdown to major mineral evolution in metamorphic rocks: a thermodynamic approach in the Na_2O–CaO–

K_2O–FeO–MgO–Al_2O_3 –SiO_2 –H_2O–TiO_2–ZrO_2 system. Journal of Metamorphic Geology **29**, 151–166

Kinny, P. D., Black, L. P. & Sheraton, J. W. (1993). Zircon ages and distribution of Archaean and Proterozoic rocks in the Rauer Island. Antarctic Science **5**, 193–206.

Korhonen, F. J., Powell, R. & Stout, J. H. (2012). Stability of sapphirine plus quartz in the oxidized rocks of the Wilson Lake terrane, Labrador: Calculated equilibria in NCKFMASHTO. Journal of Metamorphic Geology **30**, 21–36.

Lamadrid, H. M., Lamb, W. M., Santosh, M. & Bodnar, R. J. (2014). Raman spectroscopic characterization of H_2O in CO_2−rich fluid inclusions in granulite facies metamorphic rocks. Gondwana Research **26**, 301−310.

Kotková, J., Škoda, R. & Machovič, V. (2014). Kumdykolite from the ultrahigh–pressure granulite of the Bohemian Massif. American Mineralogist **99**, 1798–1801.

Lei, H. & Xu, H. (2018). A review of ultrahigh temperature metamorphism. Journal of Earth Science **29**, 1167–1180.

Li, X. C., Zhou, M. F., Chen, W. T., Zhao, X. F. & Tran, M. (2018). Uranium–lead dating of hydrothermal zircon and monazite from the Sin Quyen Fe–Cu–REE–Au–(U) deposit, northwestern Vietnam. Mineralium Deposita 53, 399–416.

Liu, P., Zhang, J., Massonne, H. J. & Jin, Z. (2018). Polyphase solid–inclusions formed by interactions between infiltrating fluids and precursor minerals enclosed in garnet of UHP rocks from the Dabie Shan, China. American Mineralogist **103**, 1663–1673.

Liu, X., Zhao, Y., Song, B., Liu, J. & Cui, J. (2009). SHRIMP U–Pb zircon geochronology of high−grade rocks and charnockites from the eastern Amery Ice Shelf and southwestern Prydz Bay, East Antarctica: Constraints on Late Mesoproterozoic to Cambrian tectonothermal events related to supercontinent assembly. Gondwana Research **16**, 342–361.

Liu, X., Wang, W–(RZ)., Zhao, Y., Liu, J. & Song, B. (2014). Early Neoproterozoic granulite facies metamorphism of mafic dykes from the Vestfold Block, east Antarctica. Journal Metamorphic Geology **32**, 1041–1062.

Liu, X., Chen, L., Wang, W–(RZ)., Zhao, Y., Ling, X. & Song, B. (2021). Deciphering early Neoproterozoic and Cambrian high–grade metamorphic events in the Archean/Mesoproterozoic Rauer Group, East Antarctica. Precambrian Research **365**, 106392.

Liu, Y. S., Hu, Z. C., Gao, S., Günther, D., Xu, J., Gao, C. G. & Chen, H. H. (2008). In situ analysis

of major and trace elements of anhydrous minerals by LA–ICP–MS without applying an internal standard. Chemical Geology **257**, 34–43.

Liu, Y. S., Gao, S., Hu, Z. C., Gao, C. G., Zong, K. Q. & Wang, D. B. (2010). Continental and oceanic crust recycling–induced melt–peridotite interactions in the Trans–North China Orogen: U–Pb dating, Hf isotopes and trace elements in zircons from mantle xenoliths. Journal of Petrology **51**, 537–571.

Liu, Z., Bartoli, O., Tong, L., Xu, Y. G. & Huang, X. (2020). Permian ultrahigh–temperature reworking in the southern Chinese Altai: Evidence from petrology, P–T estimates, zircon and monazite U–Th–Pb geochronology. Gondwana Research **78**, 20–40.

Lowenstern, J. B. (1995). Applications of silicate–melt inclusions to the study of magmatic volatiles. Magmas, Fluids, and Ore Deposits **23**, 71–99.

Ludwig, K. R. (1999). Using Isoplot/EX, Version 2. A Geological Toolkit for Microsoft Excel. Berkeley Geochronological Center, Special Publication 1a, p. 47.

Luth, W. C., Jahns, R. H. & Tuttle, O. F. (1964). The granite system at pressure of 4 to 10 kilobars. Journal of Geophysical Research **69**, 759–773.

Morgan VI, G. B. & London, D. (2005). Effect of current density on the electron microprobe analysis of alkali aluminosilicate glasses. American Mineralogist **90**, 1131–1138.

Németh, P., Lehner, S. W., Petaev, M. I. & Buseck, P. R. (2013). Kumdykolite, a high–temperature feldspar from an enstatite chondrite. American Mineralogist **98**, 1070–1073.

O'Connor, J. T. (1965). A classification for quartz–rich igneous rocks based on feldspar ratios. United States Geological Survey Professional Paper **525**, 79–84.

Pan, J.Y., Ni, P. & Wang, R. C. (2019). Comparison of fluid processes in coexisting wolframite and quartz from a giant vein–type tungsten deposit, South China: Insights from detailed petrography and LA–ICP–MS analysis of fluid inclusions. American Mineralogist **104**, 1092–1116.

Patiño Douce, A. E. & Johnston, A. D. (1991). Phase equilibria and melt productivity in the pelitic system: Implications for the origin of peraluminous granitoids and aluminous granulites. Contributions to Mineralogy and Petrology **107**, 202–218.

Phillips, G., Wilson, C. J. L., Phillips, D. & Szczepanski, S. (2007). Thermochronological (Ar/Ar) evidence of early Palaeozoic basin inversion within the southern Prince Charles Mountains, east Antarctica: implications for East Gondwana. Journal of the Geological Society, London,

164, 771–784.

Pownall, J. M., Hall, R., Armstrong, R. A. & Forster, M. A. (2014). Earth's youngest–known ultrahigh–temperature granulites discovered on Seram, eastern Indonesia. Geology **42**, 279–282.

Redler, C., White, R. W. & Johnson, T. E. (2013). Migmatites in the Ivrea Zone (NW Italy): Constraints on partial melting and melt loss in metasedimentary rocks from Val Strona di Omegna. Lithos **175**, 40–53.

Ren, L., Li, C., Wang, Y. & Liu, P. (2016). On constraining the Pan–African high–grade metamorphism time of the Larsemann Hills, East Antarctica. Chinese Journal of Polar Research **28**, 451–461 (in Chinese with English abstract).

Rosenberg, C. L. & Handy, M. R. (2005). Experimental deformation of partially melted granite revisited: implications for the continental crust. Journal of Metamorphic Geology **23**, 19–28.

Rudnick, R. L. & Gao, S. (2014). Composition of the continental crust. In: Rudnick, R.L., (Eds.), Treatise on geochemistry, 2nd edn, 1–51.

Rybach, L. (1988). Determination of heat production rate. In: Haenel, R., Rybach, L., Stegena, L. (Eds.), Handbook of Terrestrial Heat–flow Density Determination. Kluwer Academic Press, 125–142.

Santosh, M., Liu, S. J., Tsunogae, T. & Li, J. H. (2012). Paleoproterozoic ultrahigh–temperature granulites in the North China Craton: implications for tectonic models on extreme crustal metamorphism. Precambrian Research **222–223**, 77–106.

Sawant, A. D., Gupta, S., Clark, C. & Misra, S. (2017). The Rauer–Rengali connection in the Indo–Antarctica amalgam: evidence from structure, metamorphism and geochronology. In: Pant, N.C., Dasgupta, S. (Eds), Crustal Evolution of India and Antarctica: The Supercontinent Connection. Geological Society, London, 171–196.

Sawyer, E. W., Cesare, B. & Brown, M. (2011). When the Continental Crust Melts. Elements **7**, 229–234.

Scaillet, B., Holtz, F., Pichavant, M. & Schmidt, M. (1996). Viscosity of Himalayan leucogranites: Implications for mechanisms of granitic magma ascent. Journal of Geophysical Research: Solid Earth **101**, 27691–27699.

Shabeer, K. P., Satish−Kumar, M., Armstrong, R. & Buick, I. S. (2005). Constraints on the timing of Pan−African granulite−facies metamorphism in the Kerala Khondalite Belt of southern India:

SHRIMP mineral ages and Nd isotopic systematics. Journal of Geology **113**, 95–106.

Sims, J. R., Dirks, P. H. G. M., Carson, C. J. & Wilson, C. J. L. (1994). The structural evolution of the Rauer Group, East Antarctica: Mafic dykes as passive markers in a composite Proterozoic terrain. Antarctic Science **6**, 379–394.

Spreitzer, S. K., Walters, J. B., Cruz–Uribe, A., Williams, M. L., Yates, M. G., Jercinovic, M. J., Grew, E. S. & Carson, C. J. (2021). Monazite petrochronology of polymetamorphic granulite–facies rocks of the Larsemann Hills, Prydz Bay, East Antarctica. Journal of Metamorphic Geology **39**, 1205–1228.

Suzuki, K. & Kawakami, T. (2019). Metamorphic pressure−temperature conditions of the Lützow−Holm Complex of East Antarctica deduced from Zr−in−rutile geothermometer and Al_2SiO_5 minerals enclosed in garnet. Journal of Mineralogical and Petrological Sciences **114**, 267–279.

Tacchetto, T., Bartoli, O., Cesare, B., Berkesi, M., Aradi, L. E., Dumond, G. & Szabó, C. (2019). Multiphase inclusions in peritectic garnet from granulites of the Athabasca granulite terrane (Canada): Evidence of carbon recycling during Neoarchean crustal melting. Chemical Geology **508**, 197–209.

Tacchetto, T., Reddy, S. M., Bartoli, O., Rickard, W. D. A., Fougerouse, D., Saxey, D. W., Quadir, Z. & Clark, C. (2021). Pre-nucleation geochemical heterogeneity within glassy anatectic inclusions and the role of water in glass preservation. Contributions to Mineralogy and Petrology **176**, 70.

Taylor, R. J. M., Clark, C., Fitzsimons I. C. W., Santosh, M., Hand, M., Evans, N. & McDonald, B. (2014). Post–peak, fluid mediated modification of granulite facies zircon and monazite in the Trivandrum Block, southern India. Contributions to Mineralogy and Petrology **168**, 1–17.

Tong, L. & Wilson, C. J. L. (2006). Tectonothermal evolution of the ultrahigh temperature metapelites from the Rauer Group, east Antarctica. Precambrian Research **149**, 1–20.

Tong, L., Xu, Y. G., Cawood, P. A., Zhou, X., Chen, Y. & Liu, Z. (2014a). Anticlockwise P–T evolution at ~280 Ma recorded from ultrahigh–temperature metapelitic granulite in the Chinese Altai orogenic belt, a possible link with the Tarim mantle plume? Journal of Asian Earth Sciences **94**, 1–11.

Tong, L., Liu, X., Wang, Y. & Liang, X. (2014b). Metamorphic P–T paths of metapelitic granulites from the Larsemann Hills, East Antarctica. Lithos **192–195**, 102–115.

Tong, L., Liu, Z., Li, Z. X., Liu, X. & Zhou, X. (2019). Poly–phase metamorphism of garnet–bearing mafic granulite from the Larsemann Hills, East Antarctica: P–T path, U–Pb ages and tectonic implications. Precambrian Research **326**, 385–398.

Tong, L. X., Liu, Z. & Wang, Y. B. (2021). Research progress of the ultrahigh−temperature granulites in the Rauer Group, East Antarctica. Journal of Geomechanics **27**, 705−718 (in Chinese with English abstract).

Wang, W–(RZ)., Zhao, Y., Wei, C., Daczko, N. R., Liu, X., Xiao, W. & Zhang, Z. (2022). High–Ultrahigh Temperature Metamorphism in the Larsemann Hills: Insights into the Tectono–Thermal Evolution of the Prydz Bay Region, East Antarctica. Journal of Petrology **63**, 1–30.

Wang, X., Chou, M. I., Hu, W., Burruss, R. C., Sun, Q. & Song, Y. (2011). Raman spectroscopic measurements of CO_2 density: Experimental calibration with high– pressure optical cell (HPOC) and fused silica capillary capsule (FSCC) with application to fluid inclusion observations. Geochimica et Cosmochimica Acta **75**, 4080–4093.

Wang, Y., Tong, L. & Liu, D. (2007). Zircon U–Pb ages from an ultra–high temperature metapelite, Rauer Group, east Antarctica: implications for overprints by Grenvillian and Pan–African events. In: Cooper, A. K., Raymond, C.R. et al. (eds), A Keystone in a Changing World–Online Proceedings of the 10th ISAES. USGS Open–File Report 2007–1047, Short Research Paper **023**, 4.

Wang, Y., Liu, D., Chung, S. L., Tong, L. & Ren, L. (2008). SHRIMP zircon age constraining from the Larsemann Hills region, Prydz Bay, for a late Mesoproterozoic to early Neoproterozoic tectono–thermal event in east Antarctica. American Journal of Science **308**, 573–617.

Warr, L. N. (2021). IMA–CNMNC approved mineral symbols. Mineralogical Magazine **85**, 291–320.

Watt, G. R. & Harley, S. L. (1993). Accessory phase controls on the geochemistry of crustal melts and restites produced during water–undersaturated partial melting. Contributions to Mineralogy and Petrology **114**, 550–566.

Wei, C. J. (2016). Granulite facies metamorphism and petrogenesis of granite (II): Quantitative modeling of the HT–UHT phase equilibria for metapelites and the petrogenesis of S–type granite. Acta Petrologica Sinica **32**, 1625–1643 (in Chinese with English abstract).

Weinberg, R. F. & Hasalová, P. (2015). Water−fluxed melting of the continental crust: A review. Lithos **212–21**5, 158–188.

Wheller, C. J. & Powell, R. (2014). A new thermodynamic model for sapphirine: calculated phase equilibria in K_2O–FeO–MgO–Al_2O_3–SiO_2–H_2O–TiO_2–Fe_2O_3. Journal of Metamorphic Geology **32**, 287–299.

White, R. W., Powell, R. & Halpin, J. A. (2004). Spatially–focussed melt formation in aluminous metapelites from Broken Hill, Australia. Journal of Metamorphic Geology **22**, 825–845.

White, R. W., Stevens, G. & Johnson, T. E. (2011). Is the crucible reproducible? Reconciling melting experiments with thermodynamic calculations. Elements **7**, 241–246.

White, R. W., Powell, R., Holland, T. J. B., Johnson, T.E. & Green, E. C. R. (2014). New mineral activity–composition relations for thermodynamic calculations in metapelitic systems. Journal of Metamorphic Geology **32**, 261–286.

Wilson, C. J. L., Quinn, C., Tong, L. & Philips, D. (2007). Early Palaeozoic intracratonic shears and post–tectonic cooling in the Rauer Group, Prydz Bay, East Antarctica constrained by $^{40}Ar/^{39}Ar$ thermo–chronology. Antarctic Science **19**, 339–353.

Wolf, M., Romer, R. & Glodny, J. (2019). Isotope disequilibrium during partial melting of metasedimentary rocks. Geochimica et Cosmochimica Acta **257**, 163–183.

Zhang, X. Z., Wang, Q., Wyman, D., Kerr, A. C., Dan, W. & Qi, Y. (2022), Tibetan Plateau insights into >1100° C crustal melting in the Quaternary. Geology **50**, 1432–1437.

Zhao, Y., Liu, X., Song, B., Zhang, Z., Li, J., Yao, Y. & Wang, Y. (1995). Constraints on the stratigraphic age of the Larsemann Hills, East Antarctica: possible implications for Neo–Proterzoic tectonics. Precambrian Research **75**, 175–188.

Zeng, L., Asimow, P. D. & Saleeby, J. B. (2005). Coupling of anatectic reactions and dissolution of accessory phases and the Sr and Nd isotope systematics of anatectic melts from a metasedimentary source. Geochimica et Cosmochimica Acta **69**, 3671–3682.

Zajacz, Z. & Halter, W. (2007). LA–ICPMS analyses of silicate melt inclusions in co–precipitated minerals: Quantification, data analysis and mineral/melt partitioning. Geochimica et Cosmochimica Acta **71**, 1021–1040.

Zong, K. Q., Klemd, R., Yuan, Y., He, Z. Y., Guo, J. L., Shi, X. L., Liu, Y. S., Hu, Z. C. & Zhang, Z. M. (2017). The assembly of Rodinia: The correlation of early Neoproterozoic (ca. 900 Ma) high–grade metamorphism and continental arc formation in the southern Beishan Orogen, southern Central Asian Orogenic Belt (CAOB). Precambrian Research **290**, 32–48.

TABLE CAPTIONS

Table 1 Representative mineral compositions of the Mather *UHT* granulites. The major element compositions are shown in wt.%.

	Grt-c	Grt-m	Grt-r	Grt_3	$Opx_{in\ Grt}$	Opx-c	Opx-r	$Opx_{exsolved}$	Opx_{inter}	Opx_3	$Spr_{with\ Crd}$	$Spr_{with\ Bt}$	Crd inter	$Bt_{in\ Grt}$	Bt_{porphy}	Bt_{inter}	Bt-3	Pl_{inter}	Pl_3	Spl	Pl-in Zrn	Bt-in Zrn	Opx-in Zrn
SiO_2	40.94	40.51	40.63	39.94	51.14	52.34	49.11	51.07	50.20	50.68	13.27	13.41	49.20	39.71	36.67	36.69	37.48	47.03	55.19	0.04	59.87	38.51	50.28
TiO_2	0.03	0.06	0.00	0.00	0.04	0.07	0.08	0.11	0.09	0.06	0.05	0.10	0.03	3.47	4.08	4.32	4.12	0.00	0.00	0.04	0.01	3.54	0.05
Al_2O_3	23.23	23.01	23.11	22.38	8.85	6.49	9.16	6.88	7.37	7.67	62.22	61.34	34.03	15.49	16.93	17.13	16.88	33.73	29.04	61.11	24.95	16.96	6.79
Cr_2O_3	0.12	0.10	0.09	0.01	0.10	0.03	0.03	0.07	0.12	0.07	0.32	0.49	0.06	0.09	0.13	0.25	0.10	0.00	0.00	1.28	0.06	0.08	0.11
FeO^T	17.26	18.17	19.73	23.84	12.04	13.06	14.93	15.21	15.24	15.49	7.79	8.51	2.61	5.44	8.25	8.92	8.68	0.24	0.25	21.85	0.03	11.53	17.62
MnO	0.18	0.16	0.26	0.38	0.04	0.03	0.10	0.07	0.08	0.11	0.04	0.06	0.03	0.00	0.02	0.00	0.01	0.02	0.01	0.08		0.06	0.08
MgO	16.887	15.996	15.000	11.881	27.311	27.661	25.58	26.23	27.000	25.17	16.26	16.70	12.600	21.90	18.24	17.79	18.16	0.00	0.13	12.71	0.00	15.58	24.69
C	1.	1.	1.	1.	0.	0.	0	0.	0.	0	0.	0.	0.	0.	0.	0	0	1	1	0	7.	0.	0.1

aO	47	18	63	78	10	09	.11	12	09	.07	00	02	03	02	02	.00	.00	6.46	0.40	.00	15	00	0
Na_2O	0.001	0.003	0.002	0.002	0.005	0.000	0.000	0.03	0.002	0.004	0.02	0.00	0.004	0.043	0.044	0.33	0.41	2.14	5.33	0.08	7.24	0.12	0.01
K_2O	0.000	0.000	0.000	0.001	0.000	0.000	0.001	0.00	0.000	0.003	0.00	0.00	0.001	9.466	9.996	9.552	9.885	0.03	0.53	0.021	0.16	8.56	0.00
ZnO	–	–	–	–	–	–	–	–	–	–	–	–	–	–	–	–	–	–	–	1.37	–	–	–
F	–	–	–	–	–	–	–	–	–	–	–	–	–	0.37	0.09	0.29	0.22	–	–	–	–	–	–
Cl	–	–	–	–	–	–	–	–	–	–	–	–	–	0.10	0.12	0.11	0.12	–	–	–	–	–	–
Total	100.11	99.18	100.47	100.17	99.67	99.72	99.09	99.79	100.21	99.39	99.97	100.63	98.63	96.49	94.94	95.34	96.03	99.66	100.87	98.58	99.52	94.95	99.72
O	12	12	12	12	6	6	6	6	6	6	20	20	18	11	11	11	11	8	8	4	8	11	6
Si	2.9844	2.9995	2.9887	3.0009	1.8155	1.8664	1.7733	1.834	1.7791	1.8333	1.5778	1.5887	4.9211	2.8002	2.6881	2.6776	2.7110	2.1165	2.4668	0.0001	2.6679	2.8087	1.8826
Ti	0.0002	0.0003	0.0000	0.0000	0.0001	0.0002	0.0002	0.0003	0.0002	0.0002	0.0004	0.0009	0.0002	0.0184	0.0224	0.0237	0.0224	0.0000	0.0000	0.0001	0.0000	0.0194	0.0001
Al	1.999	2.000	2.000	1.998	0.037	0.027	0.03	0.2911	0.031	0.03	8.7233	8.5611	4.001	1.128	1.445	1.4	1.4	1.8	1.53	1.19	1.3166	1.4588	0.2911

	6	5	3	8	0	2	90		0	27			2	9	9	72	39	31	1	36			
Cr	0.0007	0.0006	0.0005	0.0001	0.0003	0.0001	0.001	0.002	0.003	0.002	0.030	0.046	0.005	0.005	0.008	0.015	0.006	0.000	0.000	0.027	0.002	0.004	0.003
Fe^{3+}	0.028	0.000	0.020	0.000	0.000	0.000	0.060	0.035	0.091	0.005	0.087	0.201	0.044	0.000	0.000	0.000	0.000	0.009	0.037	0.001	0.000	0.051	
Fe^{2+}	1.024	1.123	1.193	1.502	0.357	0.389	0.391	0.422	0.364	0.464	0.688	0.642	0.175	0.321	0.504	0.544	0.525	0.000	0.456	0.000	0.703	0.484	
Mn	0.011	0.010	0.016	0.024	0.001	0.001	0.003	0.002	0.002	0.003	0.004	0.006	0.003	0.000	0.001	0.000	0.001	0.000	0.002	0.001	0.004	0.002	
Mg	1.8332	1.7558	1.6444	1.3266	1.4444	1.4465	1.376	1.4044	1.4336	1.3557	2.882	2.9466	1.8778	2.3033	1.9887	1.9344	1.9577	0.000	0.509	0.000	1.692	1.337	
Ca	0.1155	0.0933	0.1288	0.1444	0.004	0.003	0.004	0.005	0.003	0.003	0.000	0.003	0.003	0.002	0.002	0.000	0.000	0.812	0.498	0.000	0.343	0.000	0.004
Na	0.001	0.004	0.003	0.003	0.003	0.000	0.000	0.002	0.001	0.003	0.005	0.000	0.008	0.058	0.063	0.047	0.058	0.191	0.462	0.004	0.628	0.017	0.000
K	0.000	0.000	0.000	0.001	0.000	0.000	0.000	0.000	0.000	0.001	0.000	0.000	0.001	0.852	0.929	0.885	0.909	0.002	0.030	0.001	0.009	0.796	0.000
Zn	–	–	–	–	–	–	–	–	–	–	–	–	–	–	–	–	–	–	–	0.	–	–	–

																				027			
F	–	–	–	–	–	–	–	–	–	–	–	–	–	0.08	0.02	0.07	0.05	–	–	–	–	–	–
Cl	–	–	–	–	–	–	–	–	–	–	–	–	–	0.01	0.02	0.01	0.02	–	–	–	–	–	–
Total	8.0000	7.9997	7.9999	7.9998	3.9998	3.9997	4.0000	4.0000	4.0003	4.0000	14.001	14.001	11.052	7.9111	7.8893	7.8883	7.8933	5.0111	5.0007	3.0002	4.9979	7.675	3.999
Alm	34	38	40	50																			
XMg	0.64	0.61	0.58	0.47	0.80	0.79	0.78	0.77	0.80	0.75	0.81	0.82	0.91	0.88	0.80	0.78	0.79			0.53		0.71	0.73
XAn																		0.81	0.50		0.35		

Abbreviations: c, core; m, mantle; r, rim; in, inclusions; inter, intergrowth; porphy, porphyroblast; 3, minerals formed at M3 stage.

Table 2 Compositions of daughter phases within NIs. The major element compositions are shown in wt.%.

	Bt	Kok	Kum
SiO_2	39.22	75.17	66.34
TiO_2	0.50	0.00	0.03
Al_2O_3	19.22	11.89	19.5
Cr_2O_3	0.18	0.00	0.01
Fe^TO	2.88	0.75	0.83
MnO	0.02	0.03	0
MgO	23.88	0.04	1.67
CaO	0.06	0.02	1.46
Na_2O	0.73	0.44	8.38
K_2O	9.29	10.85	0.71
F	0.00	–	–
Cl	0.02	–	–
Total	95.99	99.21	98.93
O	11	8	8
Si	2.729	3.345	2.934
Ti	0.026	0.000	0.001
Al	1.576	0.624	1.017
Cr	0.010	0.000	0.000
Fe^{3+}	0.025	0.028	0.031
Fe^{2+}	0.142	0.000	0.000
MnO	0.001	0.001	0.000
Mg	2.477	0.003	0.110
Ca	0.004	0.001	0.069
Na	0.098	0.038	0.719
K	0.824	0.616	0.040
F	0.000	–	–
Cl	0.002	–	–
Total	7.914	4.656	4.921
X_{Mg}	0.95		
X_{An}		0.94	0.08

1264 **Table 3** Major element concentrations of re−homogenized NIs. The compositions are shown in
1265 wt.%.

	1	2	3	4	5	6	7	8	9	10	11	12	13	14	ave.	σ	PEM
SiO_2	73.60	70.36	72.93	69.94	70.99	69.89	73.16	75.61	72.78	74.94	73.14	71.33	73.86	70.48	72.36	1.80	69.33
TiO_2	0.00	0.05	0.04	0.07	0.03	0.01	0.02	0.00	0.06	0.06	0.00	0.04	0.02	0.03	0.03	0.02	0.00
Al_2O_3	14.28	14.21	15.21	15.28	14.30	14.49	12.70	13.47	13.33	13.05	15.06	14.21	13.89	14.52	14.14	0.76	14.19
Cr_2O_3	0.00	0.04	0.00	0.00	0.00	0.02	0.00	0.01	0.00	0.00	0.00	0.03	0.00	0.02	0.01	0.01	0.00
Fe^TO	1.10	1.12	1.22	1.11	1.22	1.43	1.03	0.98	1.00	0.99	1.33	1.44	1.11	1.09	1.15	0.15	0.48
MnO	0.00	0.02	0.02	0.04	0.00	0.00	0.00	0.00	0.01	0.02	0.00	0.00	0.02	0.04	0.01	0.02	0.00
MgO	0.54	1.23	0.77	1.34	0.83	0.94	0.39	0.41	0.41	0.41	0.62	1.87	0.58	0.54	0.78	0.42	0.29
CaO	0.35	0.45	0.43	0.46	0.56	0.32	0.36	0.38	0.58	0.41	0.63	0.51	0.39	0.30	0.44	0.10	0.63
Na_2O	1.26	0.94	0.99	1.06	1.30	1.39	0.99	0.99	1.05	1.31	1.63	0.74	0.64	0.61	1.06	0.28	1.70
K_2O	6.53	8.43	6.50	8.47	6.47	7.52	7.33	6.60	7.15	6.68	5.46	7.40	7.20	8.62	7.17	0.86	8.53
Cl	0.05	0.05	0.06	0.05	0.06	0.04	0.06	0.06	0.06	0.05	0.06	0.04	0.08	0.02	0.05	0.01	0.00
P_2O_5	0.00	0.02	0.00	0.01	0.00	0.00	0.00	0.00	0.00	0.00	0.03	0.00	0.03	0.00	0.01	0.01	0.00
Total	97.71	96.91	98.18	97.84	95.76	96.05	96.04	98.51	96.44	97.92	97.95	97.61	97.80	96.29	97.21	0.89	96.29
H_2O by diff	2.29	3.09	1.82	2.16	4.24	3.95	3.96	1.49	3.56	2.08	2.05	2.39	2.20	3.71	2.79	0.89	4.85
ASI	1.46	1.24	1.61	1.30	1.41	1.32	1.24	1.42	1.26	1.29	1.55	1.40	1.45	1.33	1.40	0.11	1.08
AI	0.03	0.02	0.04	0.03	0.03	0.02	0.02	0.03	0.02	0.02	0.04	0.03	0.03	0.02	0.03	0.01	0.01
Na_2O+K_2O	7.79	9.37	7.49	9.53	7.77	8.91	8.32	7.59	8.21	7.99	7.08	8.14	7.84	9.23	8.23	0.72	10.23
K/Na	3.40	5.90	4.30	5.25	3.29	3.57	4.85	4.38	4.46	3.34	2.21	6.59	7.44	9.31	4.43	1.89	3.31
Qz norm	39.73	29.93	39.93	28.14	36.84	31.02	38.69	43.01	37.99	40.32	40.33	34.53	40.99	32.80	36.75	4.48	25.86
Crn	4.6	2.8	5.8	3.6	4.3	3.6	2.5	4.0	2.8	2.9	5.5	4.1	4.5	3.7	3.9	0.	1.0

norm	1	6	5	5	4	4	7	7	9	8	2	8	0	8	6	94	7
Or norm	39.50	51.44	39.15	51.17	39.97	46.31	45.12	39.64	43.86	40.31	32.93	44.83	43.53	52.96	43.60	5.40	52.98
Ab norm	10.95	8.21	8.58	9.19	11.47	12.22	8.76	8.52	9.26	11.36	14.07	6.41	5.52	5.36	9.27	2.45	15.12
An norm	1.76	2.19	2.19	2.23	2.90	1.63	1.89	1.91	3.01	2.08	3.01	2.55	1.81	1.54	2.19	0.48	3.28
Density	2.48	2.47	2.51	2.51	2.42	2.43	2.41	2.51	2.43	2.48	2.50	2.50	2.49	2.44	2.47	0.03	2.30
Viscosity (S96)	$10^{4.8}$	$10^{4.5}$	$10^{5.0}$	$10^{4.9}$	$10^{4.0}$	$10^{4.1}$	$10^{4.1}$	$10^{5.2}$	$10^{4.3}$	$10^{4.9}$	$10^{4.9}$	$10^{4.8}$	$10^{4.9}$	$10^{4.2}$	$10^{4.6}$	$10^{0.4}$	$10^{3.8}$
Viscosity (G08)	$10^{5.3}$	$10^{4.5}$	$10^{5.6}$	$10^{5.0}$	$10^{4.1}$	$10^{4.1}$	$10^{4.4}$	$10^{6.1}$	$10^{4.6}$	$10^{5.5}$	$10^{5.4}$	$10^{4.9}$	$10^{5.4}$	$10^{4.4}$	$10^{4.9}$	$10^{0.6}$	$10^{3.7}$
ASI values are calculated on anhydrous basis. S96, Scaillet et al. (1996); G08, Giordano et al. (2008).																	
PEM, melt compositions calculated by phase equilibria modeling at 950 ˚C with 25 mol% melts reintegrated back into bulk rock compositions.																	

Table 4 Trace element concentrations of NIs and the granulitic restite from the Mather Peninsula. The trace element compositions are shown in ppm.

	80_05	80_07	80_09	80_10	80_12	80_16	80_18	80_21	80_24	80_25	80_27	80_38	80_48	80_03*	80_08*	80_26*	80_13*	80_44*	80_46*	80_47*	80_42*	80_11*	ave.	σ	WRC
Rb	2688.8	7555.9	3887.1	7088.9	7111.7	6766.6	7327.7	2882.3	3885.7	2122.2	1566.6	1266.7	6055.0	4111.1	7988.8	1131.7	1325.0	3804.3	4892.2	1077.4	4022.1	6919.9	5778.1	3129.9	1622.4
Cs	0.9	5.6	2.6	9.5	2.8	14.7	4.6	3.2	6.9	1.8	1.8	b.d.l.	26.1	2.3	3.3	b.d.l.	15.3	3.4	9.0	35.5	3.5	2.9	7.8	8.8	1.2
Ba	1800.2	2033.0	1077.6	1433.3	2779.7	563.3	1622.3	1144.7	91.1	4467.7	3332.1	2675.5	2482.2	1597	3983.3	2364.7	4328	4002.3	5656.6	4833.7	3733.7	2751.1	3677.7	4577.2	7699.5
Li	18.8	b.d.l.	13.5	46.5	31.5	b.d.l.	42.7	b.d.l.	27.8	b.d.l.	16.0	b.d.l.	21.5	8.6	76.9	200.8	38.8	b.d.l.	17.8	b.d.l.	33.9	b.d.l.	42.5	47.0	15.6
Pb	7.2	10.4	6.3	b.d.l.	10.1	5.8	b.d.l.	8.9	3.9	9.9	10.1	8.6	12.8	*n.c*	*n.c*	*n.c*	*n.c*	*n.c*	*n.c*	*n.c*	*n.c*	*n.c*	8.5	2.4	2.1
Th	0.7	0.4	b.d.l.	0.8	b.d.l.	b.d.l.	b.d.l.	0.6	b.d.l.	3.8	2.8	3.0	1.7	*n.c*	*n.c*	*n.c*	*n.c*	*n.c*	*n.c*	*n.c*	*n.c*	*n.c*	1.7	1.2	4.5
U	4.8	5.2	2.3	4.9	6.4	1.6	0.6	2.1	1.8	8.7	6.3	6.8	9.3	*n.c*	*n.c*	*n.c*	*n.c*	*n.c*	*n.c*	*n.c*	*n.c*	*n.c*	4.7	2.7	0.4
Nb	9.	8.	5.	6.	15	4.	7.	8.	4.	14	8.	11	8.	*n.c*	*n.c*	*n.c*	*n.c*	*n.c*	*n.c*	*n.c*	*n.c*	*n.c*	8.	3.	15

	3	7	6	2	.7	2	8	4	0	.3	4	.6	0									6	4	.4
Ta	3.2	3.2	1.4	b.d.l.	b.d.l.	b.d.l.	2.0	1.8	2.0	3.2	b.d.l.	1.8	2.7	*n.c*	*n.c*	*n.c*	*n.c*	*n.c*	*n.c*	*n.c*	*n.c*	2.4	0.7	1.0
Ti	997.5	1052.6	793.0	963.1	904.3	334.2	419.1	470.5	274.1	734.6	654.5	705.3	314.5	*n.c*	*n.c*	*n.c*	*n.c*	*n.c*	*n.c*	*n.c*	*n.c*	662.9	265.1	*n.c*
Ce	7.3	10.0	7.0	6.7	5.5	4.1	b.d.l.	3.0	2.4	13.4	5.8	12.8	8.9	*n.c*	*n.c*	*n.c*	*n.c*	*n.c*	*n.c*	*n.c*	*n.c*	7.2	3.4	16.8
Sr	16.6	17.8	11.4	17.0	24.8	8.2	14.1	10.2	7.2	27.6	19.0	17.9	20.0	*n.c*	*n.c*	*n.c*	*n.c*	*n.c*	*n.c*	*n.c*	*n.c*	16.3	5.8	19.0
Nd	7.2	16.7	10.0	b.d.l.	22.8	8.3	b.d.l.	b.d.l.	b.d.l.	16.8	9.7	18.7	15.2	*n.c*	*n.c*	*n.c*	*n.c*	*n.c*	*n.c*	*n.c*	*n.c*	13.9	5.0	7.1
Sm	5.5	12.6	7.4	27.2	11.8	b.d.l.	b.d.l.	b.d.l.	b.d.l.	19.0	11.1	15.3	b.d.l.	*n.c*	*n.c*	*n.c*	*n.c*	*n.c*	*n.c*	*n.c*	*n.c*	13.7	6.4	1.8
Zr	194.9	185.1	172.9	173.9	197.0	84.2	206.3	163.8	121.1	256.0	276.5	182.8	96.2	*n.c*	*n.c*	*n.c*	*n.c*	*n.c*	*n.c*	*n.c*	*n.c*	177.8	47.7	84.9
Hf	10.7	9.7	b.d.l.	b.d.l.	2.6	b.d.l.	9.0	b.d.l.	b.d.l.	12.5	5.9	5.4	12.7	*n.c*	*n.c*	*n.c*	*n.c*	*n.c*	*n.c*	*n.c*	*n.c*	8.6	3.4	2.2
Eu	b.	2.	b.	b.	b.	b.	b.	b.	3.	b.	b.	b.	b.	*n.c*	*n.c*	*n.c*	*n.c*	*n.c*	*n.c*	*n.c*	*n.c*	2.	0.	0.

	d.l.	2	d.l.	d.l.	d.l.	d.l.	d.l.	d.l.	4	d.l.	d.l.	d.l.	d.l.									8	6	5
Gd	6.3	b.d.l.	11.9	b.d.l.	b.d.l.	17.1	b.d.l.	21.9	b.d.l.	b.d.l.	b.d.l.	23.9	25.1	*n.c*	*n.c*	*n.c*	*n.c*	*n.c*	*n.c*	*n.c*	*n.c*	*n.c*	17.7	6.8	2.6
V	b.d.l.	b.d.l.	52.0	b.d.l.	b.d.l.	29.4	18.6	101.1	55.5	35.8	46.1	79.7	146.6	*n.c*	*n.c*	*n.c*	*n.c*	*n.c*	*n.c*	*n.c*	*n.c*	*n.c*	62.7	38.1	274.7
Ga	b.d.l.	33.2	42.4	25.7	35.7	34.3	70.5	50.7	27.1	18.8	26.9	32.8	55.3	*n.c*	*n.c*	*n.c*	*n.c*	*n.c*	*n.c*	*n.c*	*n.c*	*n.c*	37.8	14.0	25.9
Zn	b.d.l.	83.3	b.d.l.	b.d.l.	b.d.l.	119.8	b.d.l.	b.d.l.	b.d.l.	b.d.l.	b.d.l.	b.d.l.	130.7	*n.c*	*n.c*	*n.c*	*n.c*	*n.c*	*n.c*	*n.c*	*n.c*	*n.c*	111.2	20.3	114.9
Sc	b.d.l.	b.d.l.	12.4	b.d.l.	b.d.l.	b.d.l.	b.d.l.	42.0	b.d.l.	b.d.l.	9.7	13.5	b.d.l.	*n.c*	*n.c*	*n.c*	*n.c*	*n.c*	*n.c*	*n.c*	*n.c*	*n.c*	19.4	13.1	19.0
Trapped phases														Apt	Mnz	Apt; Zrn	Mnz	Rt	Rt; Mnz	Rt	Rt	Rt			
Rb/Sr	16.21	42.48	33.93	41.79	28.65	82.46	52.08	27.74	53.71	7.69	8.22	7.08	30.25										33.3	20.9	8.56
Sm/	0.7	0.7	0.7		0.5					1.1	1.1	0.8											0.8	0.2	0.2

Nd	6	6	4		2					3	4	2												5
U/Th	6.62	14.47		6.39				3.74		2.27	2.22	2.27	5.47									5.4	3.8	0.09

b.d.l. below detection limit; *n.c* not considered; WRC, whole-rock composition; * Nanogranitoid inclusions with accidentally trapped phases such as zircon, monazite, apatite and rutile.

1309 **Table 5** LA−ICP−MS analysis results for zircons from the Mather *UHT* granulites.

Spot	Th (ppm)	U (ppm)	Th/U	$^{206}Pb/^{238}U$	1σ	$^{207}Pb/^{206}Pb$	1σ	$^{207}Pb/^{235}U$	1σ	$^{206}Pb/^{238}U$ (Ma)	1σ	$^{207}Pb/^{206}Pb$ (Ma)	1σ	$^{207}Pb/^{235}U$ (Ma)	1σ
Rim															
1	49	145	0.34	0.076	###	0.060	0.004	0.633	###	472	8	611	157	498	25
2	45	167	0.27	0.080	###	0.057	0.003	0.621	###	497	8	480	120	490	20
3	40	143	0.28	0.081	###	0.059	0.004	0.656	###	500	9	565	136	512	25
4	98	437	0.22	0.081	###	0.062	0.003	0.699	###	502	7	676	96	538	18
5	47	420	0.11	0.091	###	0.065	0.003	0.842	###	564	##	770	96	620	24
6	57	271	0.21	0.092	###	0.061	0.003	0.774	###	569	##	657	100	582	20
Mantle															
7	8	877	0.01	0.099	###	0.062	0.002	0.848	###	607	5	661	66	624	13
8	23	481	0.05	0.101	###	0.062	0.003	0.920	###	623	##	687	95	662	32
9	18	####	0.02	0.120	###	0.068	0.002	1.136	###	730	8	865	65	771	18
10	32	659	0.05	0.120	###	0.067	0.002	1.115	###	730	8	843	70	761	18
11	18	811	0.02	0.121	###	0.066	0.002	1.110	###	735	8	1200	71	758	18
12	22	####	0.02	0.122	###	0.066	0.002	1.123	###	743	7	817	59	765	15
13	48	524	0.09	0.123	###	0.070	0.002	1.210	###	750	##	937	67	805	21
14	42	521	0.08	0.124	###	0.065	0.002	1.115	###	754	##	759	70	760	21
15	31	####	0.03	0.130	###	0.072	0.002	1.301	###	788	9	983	55	846	16
16	21	955	0.02	0.130	###	0.070	0.002	1.273	###	788	9	943	54	834	16
17	42	848	0.05	0.131	###	0.072	0.002	1.310	###	793	9	981	56	850	17
18	15	821	0.02	0.133	###	0.067	0.00	1.245	###	806	#	835	61	821	2

					#		2		#		#				0
19	12	675	0.02	0.133	###	0.068	0.00	1.257	###	807	9	861	72	827	1
					#		2		#						9
20	43	666	0.06	0.133	###	0.073	0.00	1.376	###	808	#	1013	70	879	2
					#		3		#		#				7
21	14	####	0.01	0.136	###	0.071	0.00	1.345	###	822	8	955	49	865	1
					#		2		#						5
22	22	825	0.03	0.138	###	0.076	0.00	1.448	###	836	7	1087	55	909	1
					#		2		#						7
23	10	548	0.02	0.139	###	0.073	0.00	1.421	###	837	#	1020	54	898	2
					#		2		#		#				0
24	21	765	0.03	0.139	###	0.072	0.00	1.384	###	838	#	977	61	882	1
					#		2		#		#				7
25	24	####	0.02	0.145	###	0.069	0.00	1.391	###	873	#	889	57	885	1
					#		2		#		#				8
26	47	758	0.06	0.148	###	0.073	0.00	1.552	###	889	#	1013	67	951	3
					#		2		#		#				0
27	10	####	0.01	0.151	###	0.069	0.00	1.456	###	908	9	898	56	912	1
					#		2		#						5
28	20	####	0.01	0.152	###	0.076	0.00	1.654	###	915	#	1098	57	991	2
					#		2		#		#				6
29	23	944	0.02	0.157	###	0.078	0.00	1.708	###	940	#	1139	57	1012	2
					#		2		#		#				1
30	26	972	0.03	0.160	###	0.081	0.00	1.820	###	954	#	1232	56	1053	2
					#		2		#		#				0
31	27	805	0.03	0.161	###	0.078	0.00	1.783	###	964	#	1158	55	1039	2
					#		2		#		#				2
32	19	707	0.03	0.167	###	0.078	0.00	1.924	###	994	#	1154	64	1090	4
					#		3		#		#				0
33	21	####	0.02	0.177	###	0.084	0.00	2.069	###	1050	7	1292	40	1139	1
					#		2		#						4
Core															
34	###	529	0.28	0.330	###	0.129	0.00	6.343	###	1840	#	2088	56	2024	5
					#		4		#		#				3
35	###	219	0.79	0.393	###	0.150	0.00	8.258	###	2135	#	2340	53	2260	3
					#		5		#		#				8
36	###	351	0.69	0.394	###	0.151	0.00	8.407	###	2140	#	2361	48	2276	3
					#		4		#		#				3
37	58	289	0.20	0.367	###	0.152	0.00	7.803	###	2017	#	2374	41	2209	2
					#		4		#		#				2
38	###	144	0.70	0.382	###	0.153	0.00	8.080	###	2085	#	2381	44	2240	2
					#		4		#		#				4
39	###	167	0.83	0.453	###	0.154	0.00	9.704	###	2410	#	2387	57	2407	3

					#		5		#		#				1
40	###	378	0.57	0.371	### #	0.154	0.004	7.970	### #	2035	##	2391	39	2228	21
41	80	140	0.57	0.441	### #	0.155	0.005	9.582	### #	2355	##	2406	54	2395	30
42	###	441	1.81	0.391	### #	0.160	0.004	8.661	### #	2126	##	2452	46	2303	25
43	###	337	0.69	0.446	### #	0.160	0.004	9.951	### #	2376	##	2461	41	2430	23
44	50	49	1.01	0.436	### #	0.161	0.006	9.656	### #	2331	##	2465	58	2403	32
45	###	234	0.59	0.448	### #	0.168	0.004	10.468	### #	2384	##	2540	38	2477	24
46	###	227	0.52	0.458	### #	0.177	0.004	11.225	### #	2429	##	2623	39	2542	23

FIGURE CAPTIONS

Figure 1 (a) Simplified geological map of the Rauer Islands, East Antarctica (after Harley & Fitzsimons, 1991; Tong & Wilson, 2006; Tong et al., 2021). The black dashed line represents the boundary between Mesoproterozoic and Archean crustal components. (b) Location of the Rauer Islands in the reconstructed Gondwana supercontinent at ~500 Ma (modified after Fitzsimons, 2000; Wilson et al., 2007; Hokada et al., 2016). (c) Lithological distribution and sample locality on the Mather Peninsula (after Harley, 1998b; Hokada et al., 2016).

Figure 2 (a) A Field photograph showing the occurrence of *UHT* granulites from the Mather Peninsula, East Antarctica. (b) and (c) Enlarged photographs of white boxes in (a) displaying the presence of different lithological components. The sampling sites are shown by orange stars. The hammer for scale is 25 cm in length. (d) A representative hand specimen of the studied rocks. The coin for scale is about 2.4 cm in diameter.

Figure 3 Plane polarized light photomicrographs and BSE images of the Mather *UHT* granulite sample RG16−80. (a) Co–existence of garnet and orthopyroxene porphyroblasts. High−Al orthopyroxene inclusion within garnet is outlined by green dashed lines in the figure, which coexists with primary NIs (outlined by red dashed lines). Also shown in this figure are secondary FIs, highlighted with blue dashed lines. (b) Coexistence of biotite and orthopyroxene porphyroblasts, with a biotite inclusion within orthopyroxene. (c) K–feldspar grain rimmed by the intergrowth of orthopyroxene + cordierite + plagioclase. (d) Garnet and orthopyroxene porphyroblasts separated by fine–grained intergrowths of orthopyroxene + cordierite. (e) A BSE image showing the intergrowth of orthopyroxene + cordierite + plagioclase around garnets. (f) Intergrowths of sapphirine + cordierite in the matrix. (g) BSE image showing vermicular low–Al orthopyroxene in the rim of a high–Al orthopyroxene porphyroblast. (h) Biotite + plagioclase symplectites surrounding orthopyroxene. (i) Elongated garnet, cordierite, biotite, plagioclase in strongly deformed domains. Interstitial plagioclase is outlined by dashed black lines while quartz inclusions within garnets are highlighted with white dashed lines.

Figure 4 (a) Garnet grain showing the analysis positions. (b) Compositional zoning profile across garnet from core to rim. (c) Chondrite−normalized REE patterns of garnets for the NI−bearing and NI–absent domains. (d) Compositional zoning profiles across an orthopyroxene porphyroblast.

Figure 5 Plane polarized light photomicrographs and BSE images of NIs within garnet porphyroblasts and Raman spectrum of these inclusions. (a) Garnet crystal mounted on an epoxy resin disc containing abundant NIs. (b) and (c) Plane polarized photomicrographs showing NIs within peritectic garnets. (d)−(f) BSE images showing NIs with daughter phases of quartz, biotite and kokchetavite. Some cavities are also observed and might be related to the exsolution of fluid during the retrograde crystallization of melt. (g) Mixed Raman spectrum of NIs and their garnet hosts.

Figure 6 A BSE image of a nanogranitoid inclusion and corresponding X–ray maps of Si, Al, Mg, K and Na.

Figure 7 (a)–(c) Secondary FIs within garnet and orthopyroxene porphyroblasts. Pink and green arrows respectively point to nanogranitoid and fluid inclusions, where NIs are randomly distributed while FIs are mostly present along the cracks. (d−f) Mixed spectra of FIs and their hosts.

Figure 8 BSE images of experimentally re−homogenized NIs under 1000 °C and 12 kbar with a run duration of 6 hours (a), 950 °C and 12 kbar with run durations of 4 hours (b, d), 2 hours (c, e), and 1 hour (f). Perfectly re−homogenized inclusions with well–developed negative shapes are shown in Figures e and f. Other inclusions show clear evidence for overheating (a–d).

Figure 9 Plot of aluminum saturation index vs. alkalinity index [AI = molar Al_2O_3−(Na_2O+K_2O) (from Frost & Frost, 2008). Dotted line separates the compositional fields of I− and S−type granites (from Chappell, 1999).

KKB, Kerala Khondalite Belt (India) (Cesare et al., 2009; Ferrero et al., 2012), with peak *P*−*T* conditions of 900°C and 6−8 kbar (Cenki et al., 2002; Shabeer et al., 2005); Grf Type−A and −C, type−A or −C granulites from the Gruf Complex (European Central Alps) (Gianola et al., 2021),

with peak *P*−*T* conditions of 920−940 °C and 8.5−9.5 kbar (Galli et al., 2012); Iv, metapelitic migmatites from the Ivrea Zone (NW Italy) (Carvalho et al., 2019), with *P*−*T* conditions of 650−730 °C and 3.5−6.5 kbar for the UA, and 900−950 °C and 11−12 kbar for the G (Redler et al., 2013; Ewing et al., 2013). UA, upper amphibolite facies zone; Tr, transition zone; G, granulite facies zone.

Figure 10 (a) CIPW Qz−Ab−Or diagram showing normative compositions of analyzed NIs (normalized to 100% on anhydrous basis). Pink dashed lines show the eutectic points and cotectic lines for the subaluminous haplogranite system at a_{H2O} = 1 and different pressures (Luth, et al., 1964). References to experimental glasses: PDJ91 (shown in green), 950 °C and 7 kbar (Patiño Douce & Johnston 1991); D03 (shown in blue), 900 °C and 5 kbar (Droop et al., 2003). (b) An–Or–Ab diagram showing the normative compositions of analyzed NIs (after O'Connor, 1965).
For the symbols, please refer to Figure 9.

Figure 11 Trace element compositions of NIs and granulitic restite, normalized to the average upper continental crust (UCC) composition (data from Rudnick & Gao 2014). Trace elements of matrix glasses within metapelitic enclaves from El Hoyazo (SE Spain) (samples HO−50A, −33A and −54; Acosta−Vigil et al., 2010) are also shown for comparison. Note that peak *P*−*T* conditions for the metapelitic enclaves from El Hoyazo are 850 ± 50 ℃ and 5−7 kbar, slightly lower than the investigated rocks in this study.

Figure 12 (a) CL images of representative zircons mounted on epoxy resins. Green circles represent analyzed spots and the nearby blue numbers represent their isotopic dates. (b)−(d) Photographs showing inclusions within zircons. (e) Concordia diagram showing the results of U−Pb zircon dating. (f) Enlarged concordia diagram of the box in Figure e.

Figure 13 (a) *P*–*T* pseudosection calculated at $X(Fe_2O_3) = Fe^{3+}/Fe^{T}$ = 0.35, with a *P*−*T* range of 3−15 kbar and 750−1200 ℃. The fluid−absent solidus is shown in red dashed curves and the interpreted peak *P*−*T* conditions are shown in pale yellow. The grey curves in Figure a represent the inferred *P*−*T* path. (b) Enlarged *P*–*T* pseudosection with a *P*−*T* range of 5−9 kbar and 800−1000 ℃.

The constrained $P-T$ fields for the M2 and M3 stage are outlined by purple and black bold lines, respectively.

Figure 14 (a) $T-X_{melt}$ pseudosection showing the pre−peak evolution of the investigated rocks. Average re−homogenized nanogranitoid compositions are adopted as the melt compositions. The pressure is fixed at ~12.5 kbar. (b) Reconstructed $P-T$ pseudosection after 25% melt reintegration into the bulk rock composition.

Figure 15 Suggested $P-T$ path of *UHT* granulites from the Mather Peninsula, East Antarctica. Also shown are previously retrieved $P-T$ paths for the *UHT* granulites from the Rauer Islands (modified after Tong et al, 2021).

Fig. 1.

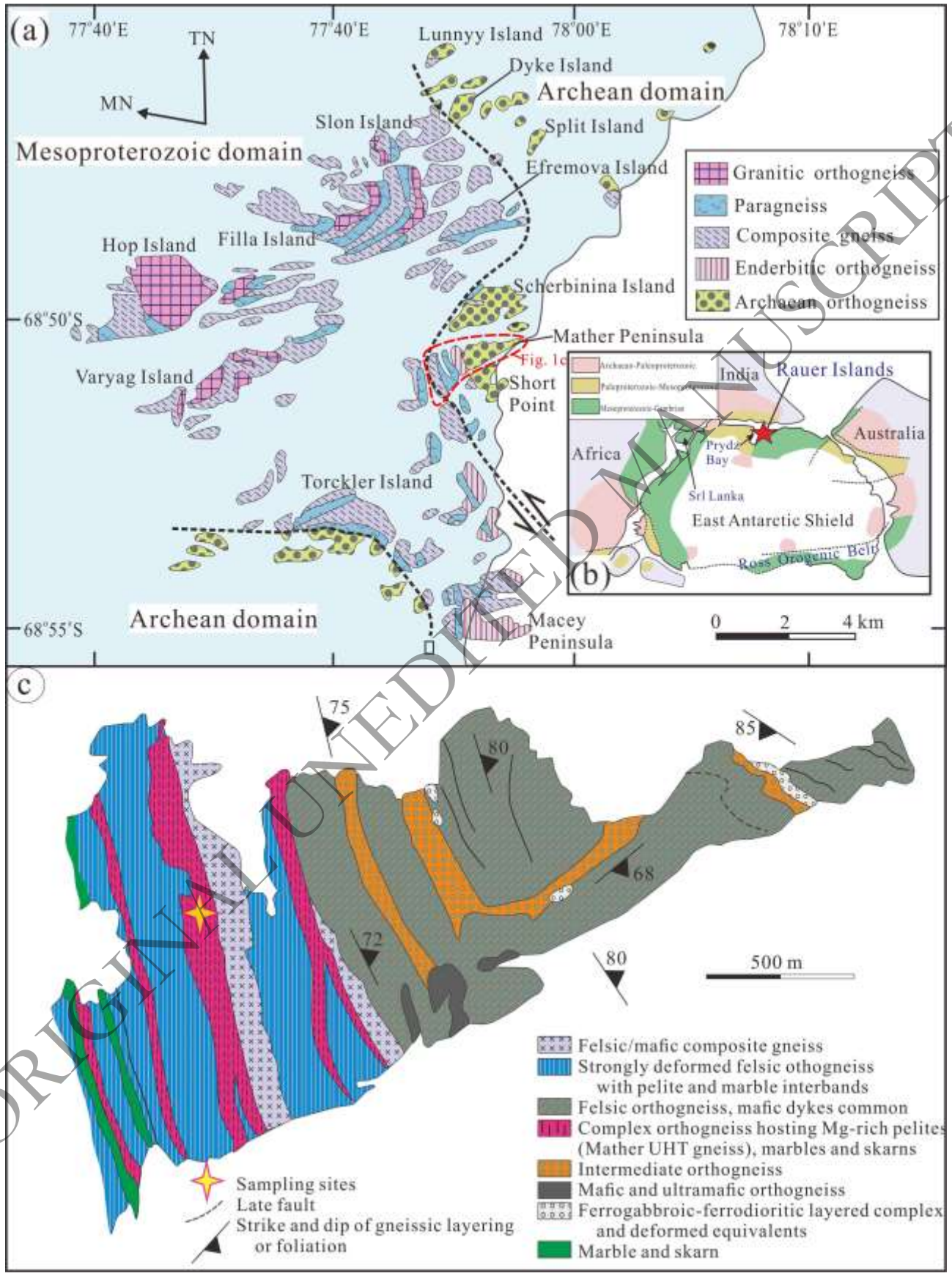

Fig. 2.

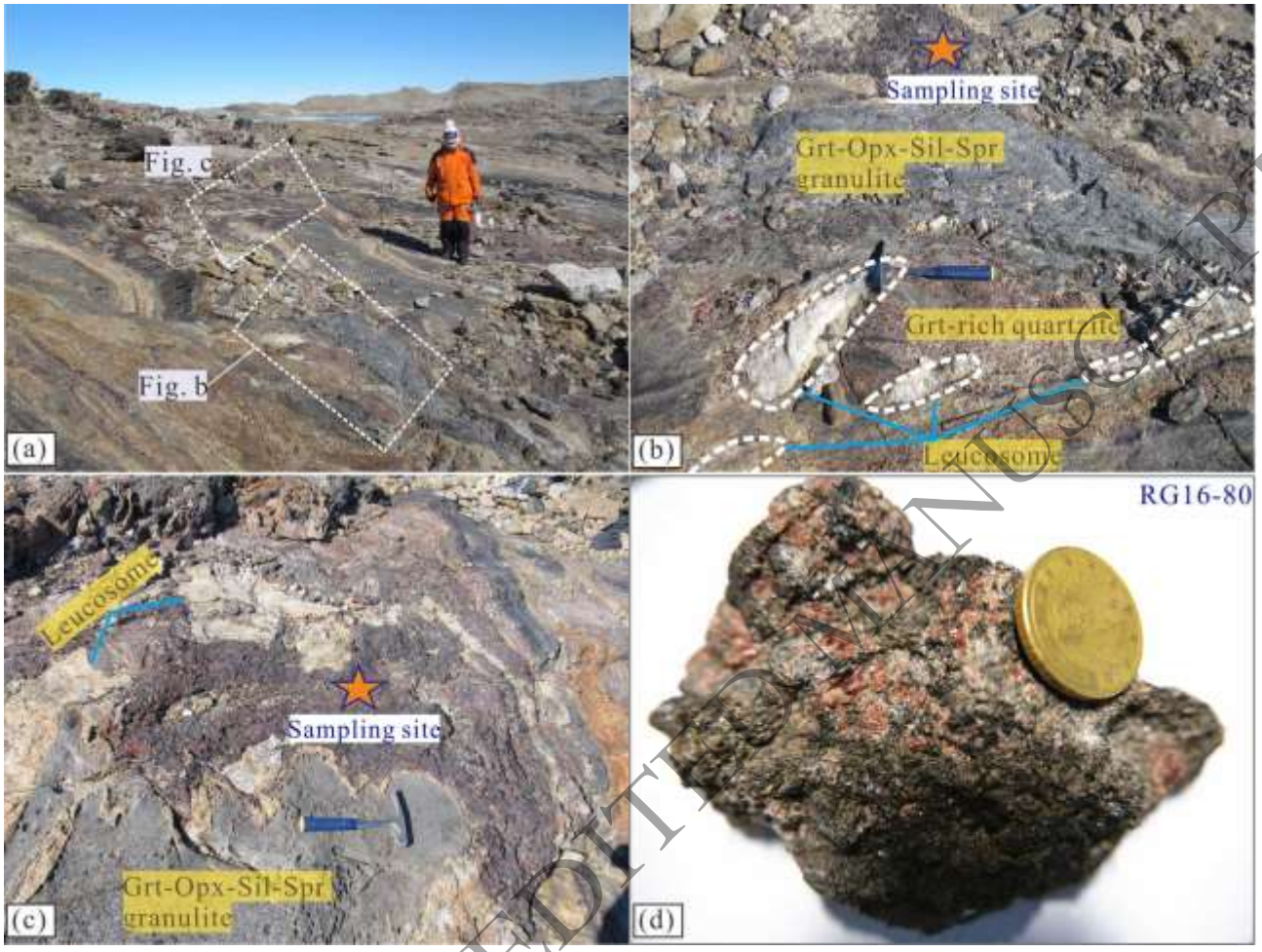

Fig. 3.

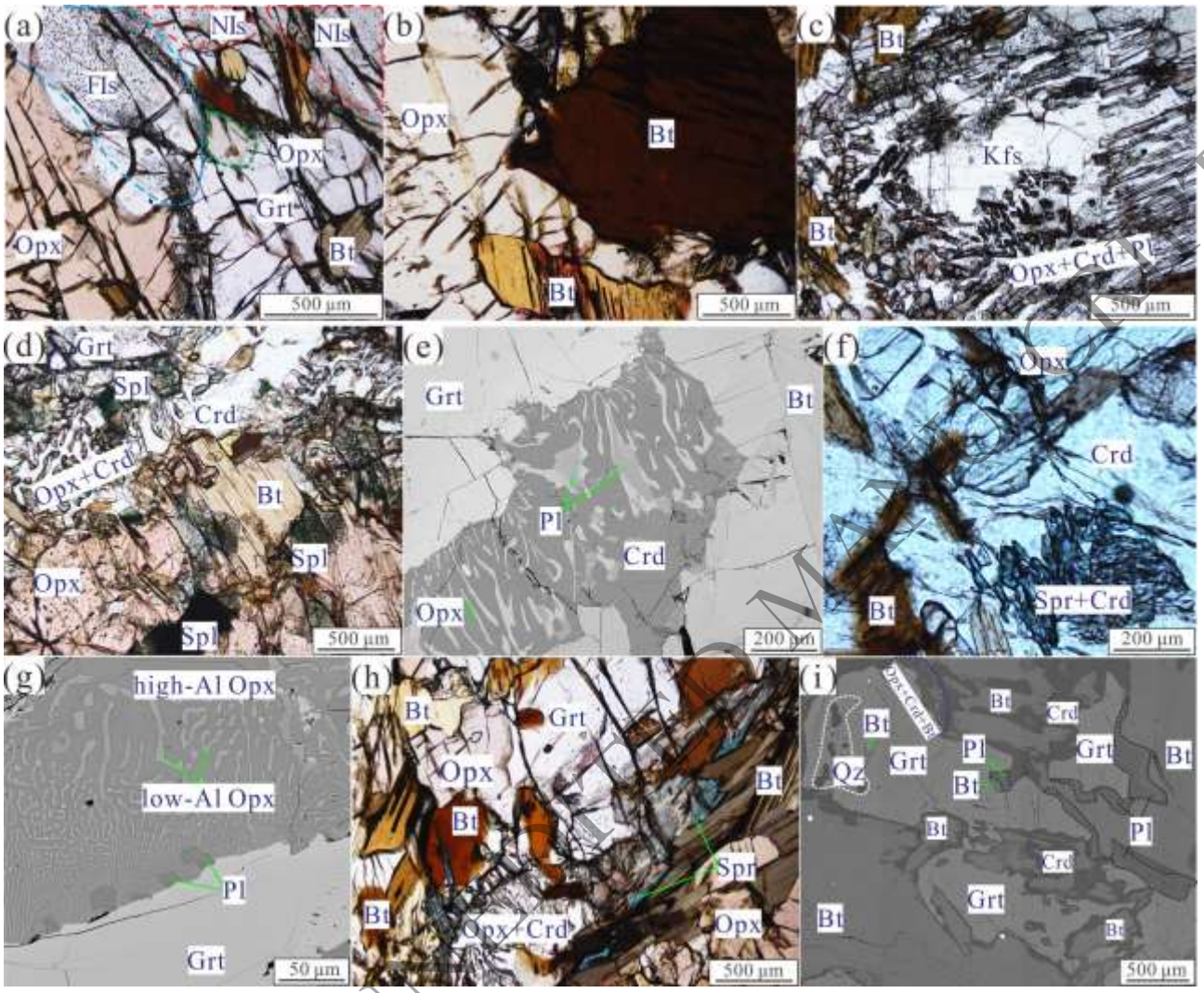

Fig. 4.

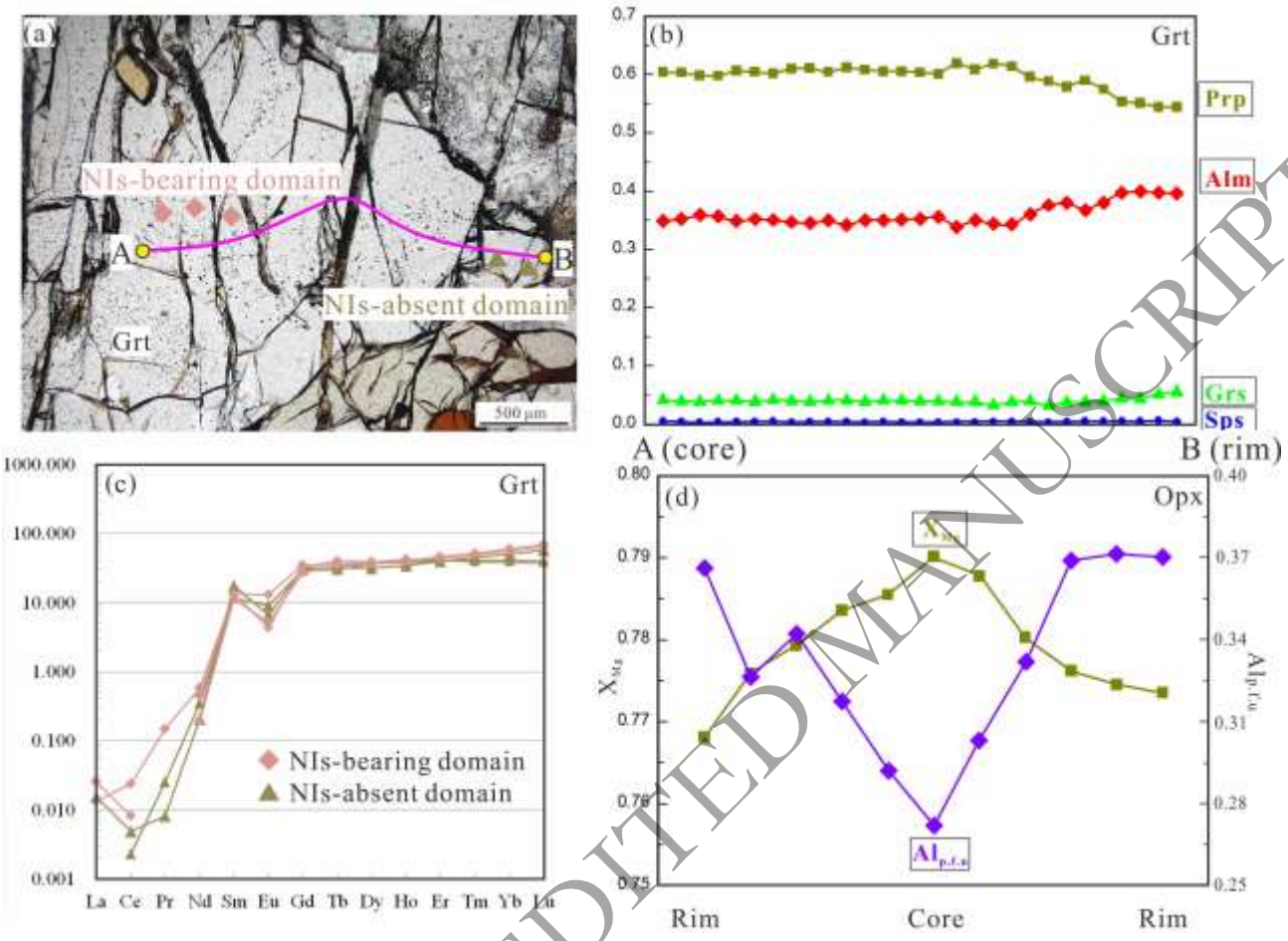

Fig. 5.

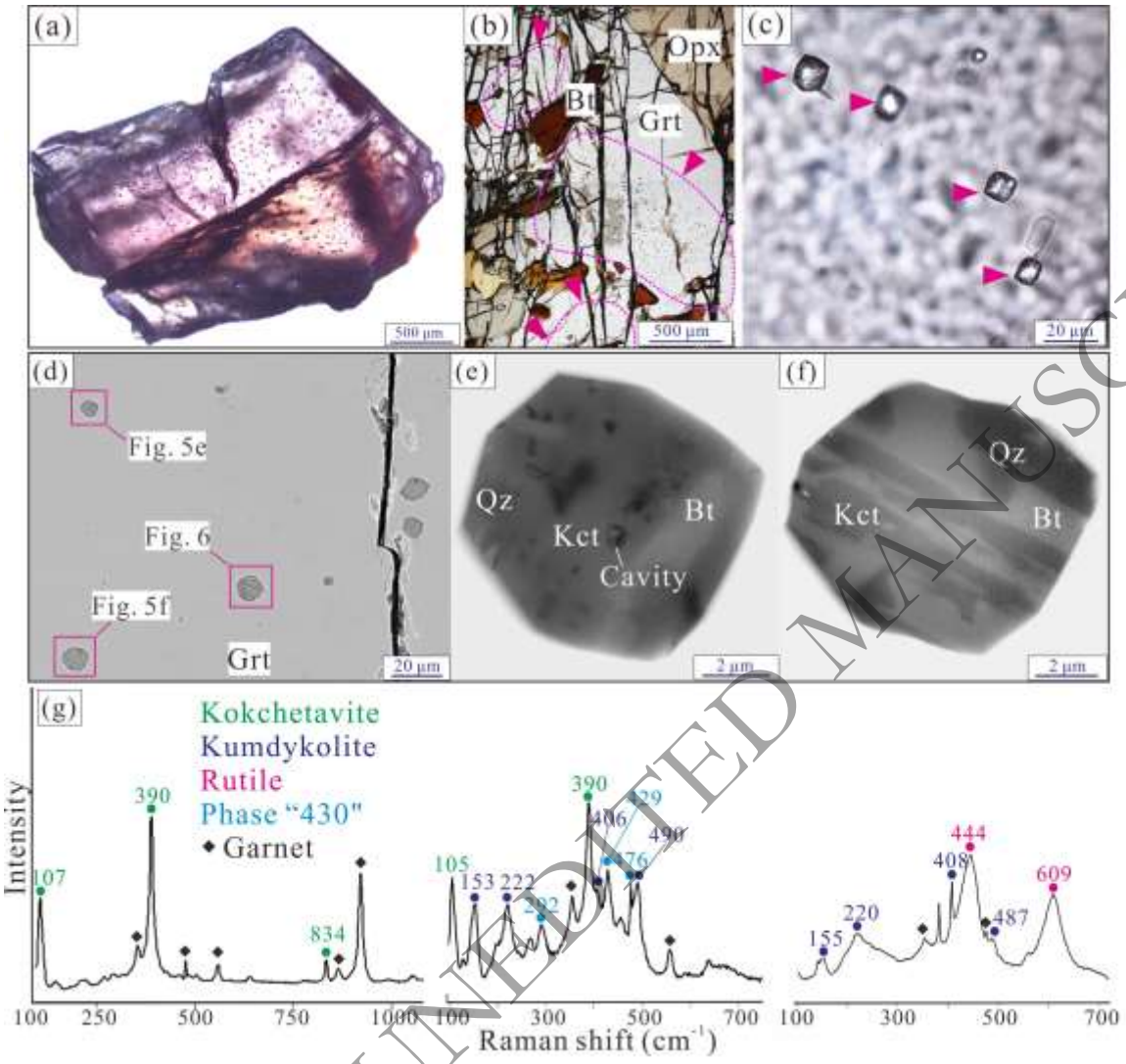

Fig. 6.

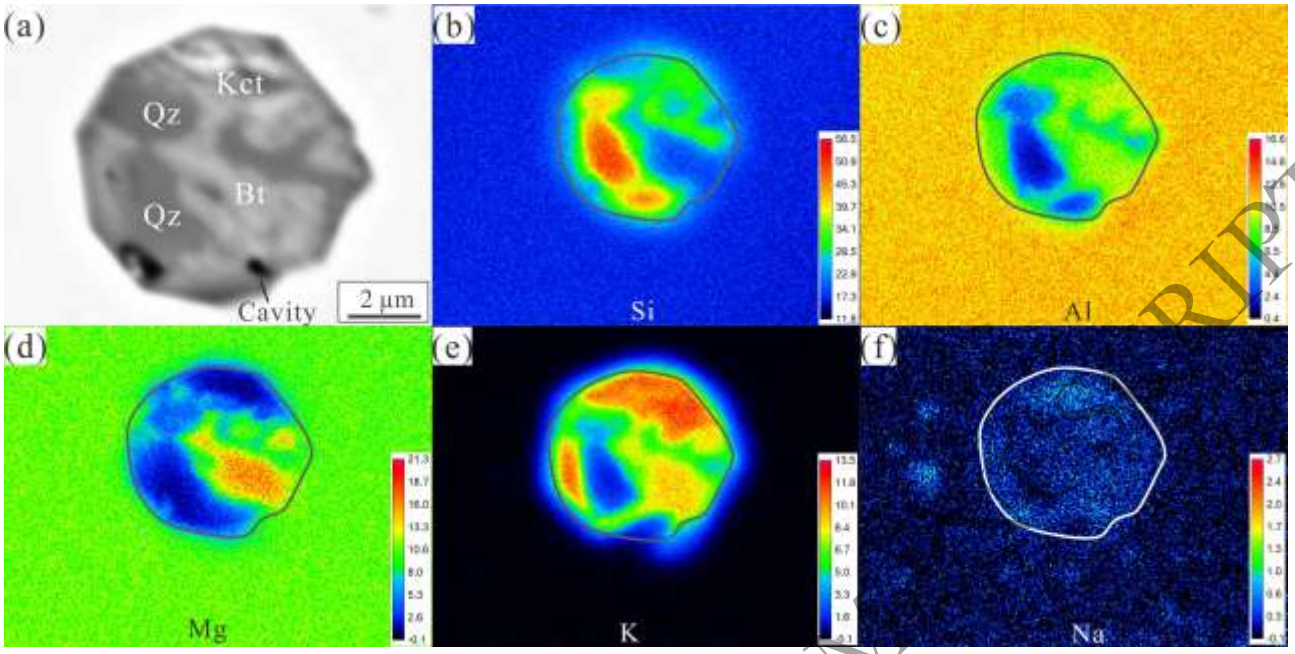

Fig. 7.

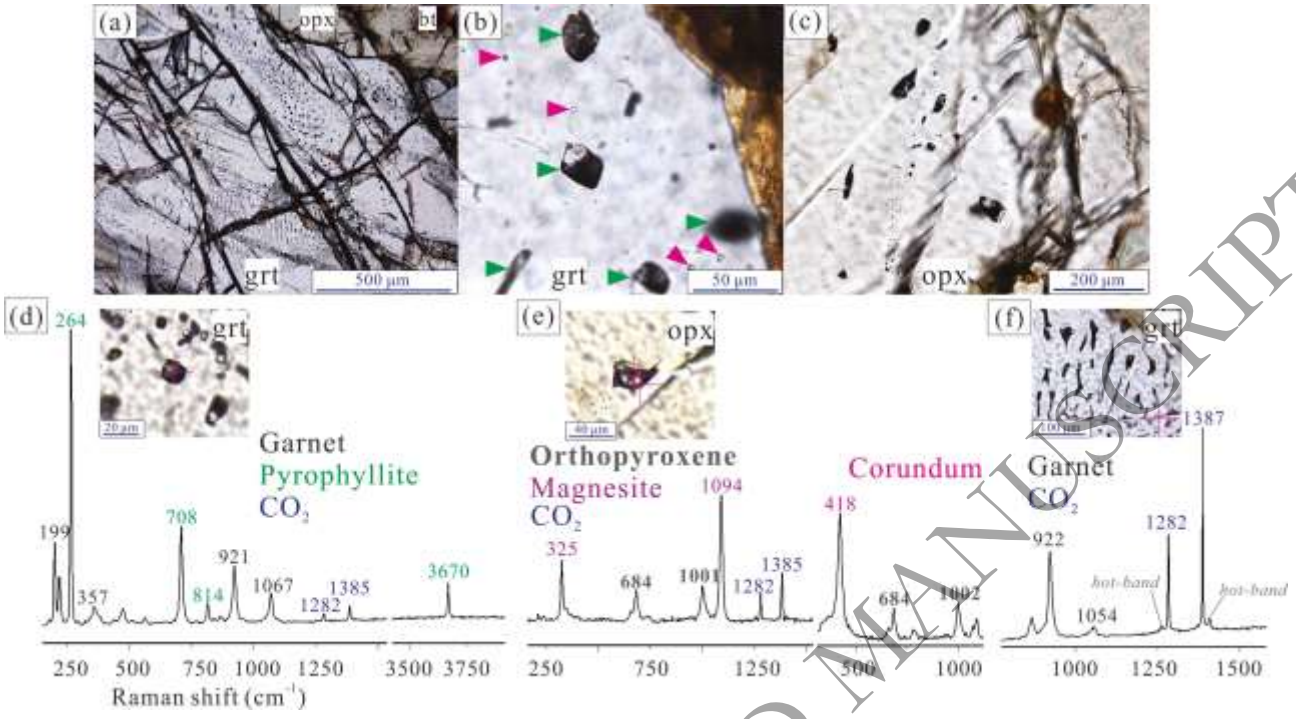

Fig. 8.

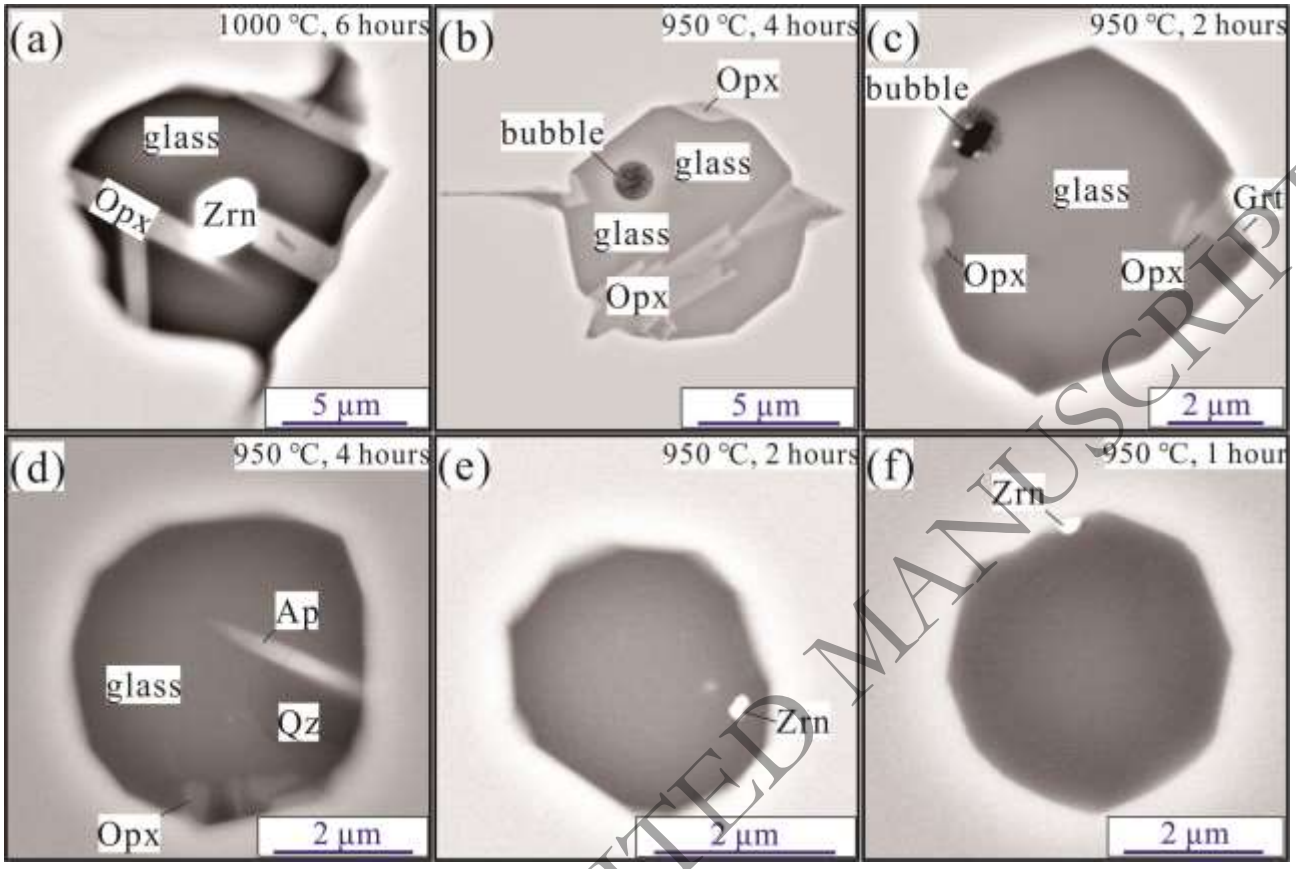

1564 **Fig. 9.**

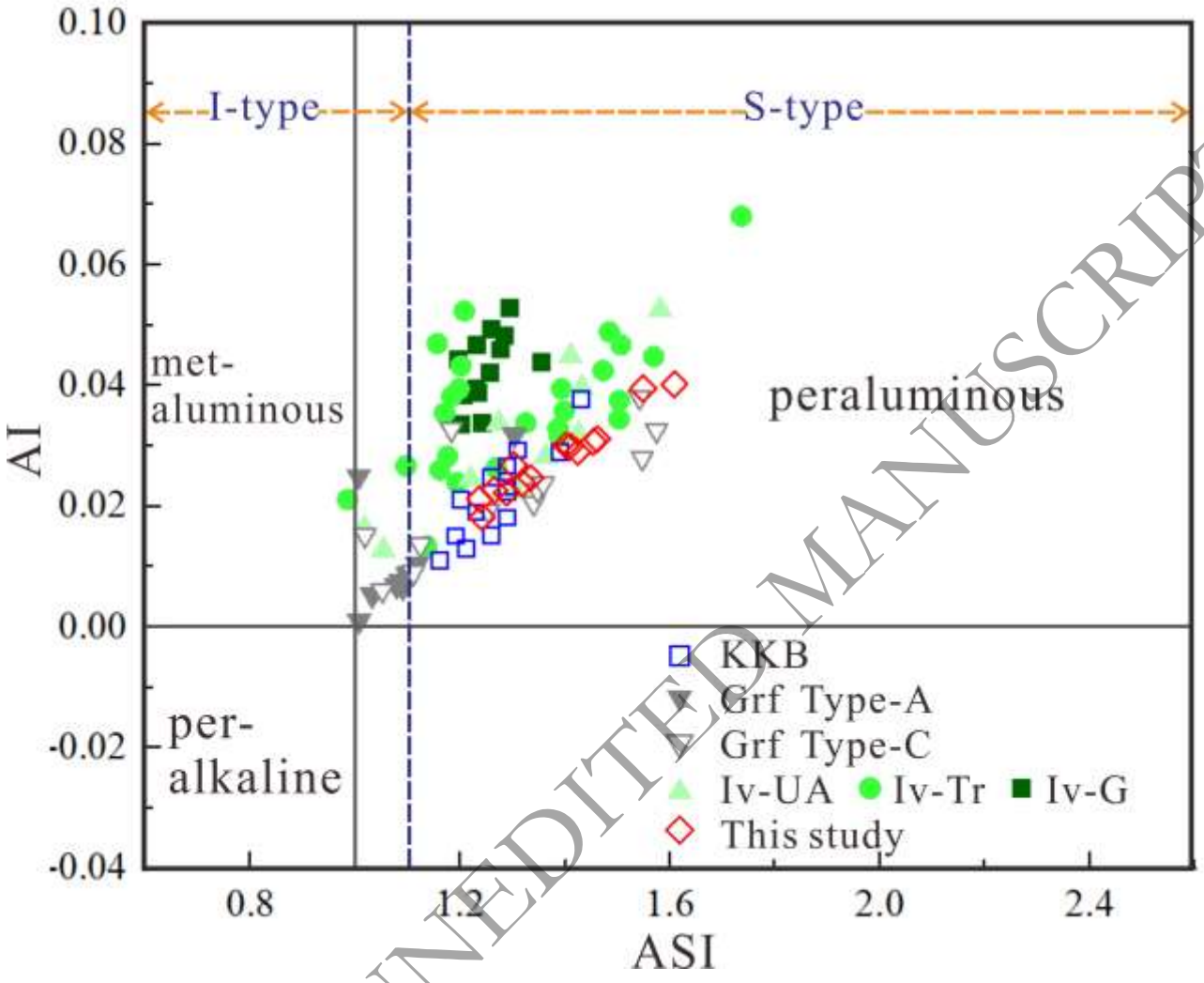

1565
1566
1567
1568
1569
1570
1571
1572
1573
1574
1575
1576

1577 **Fig. 10.**

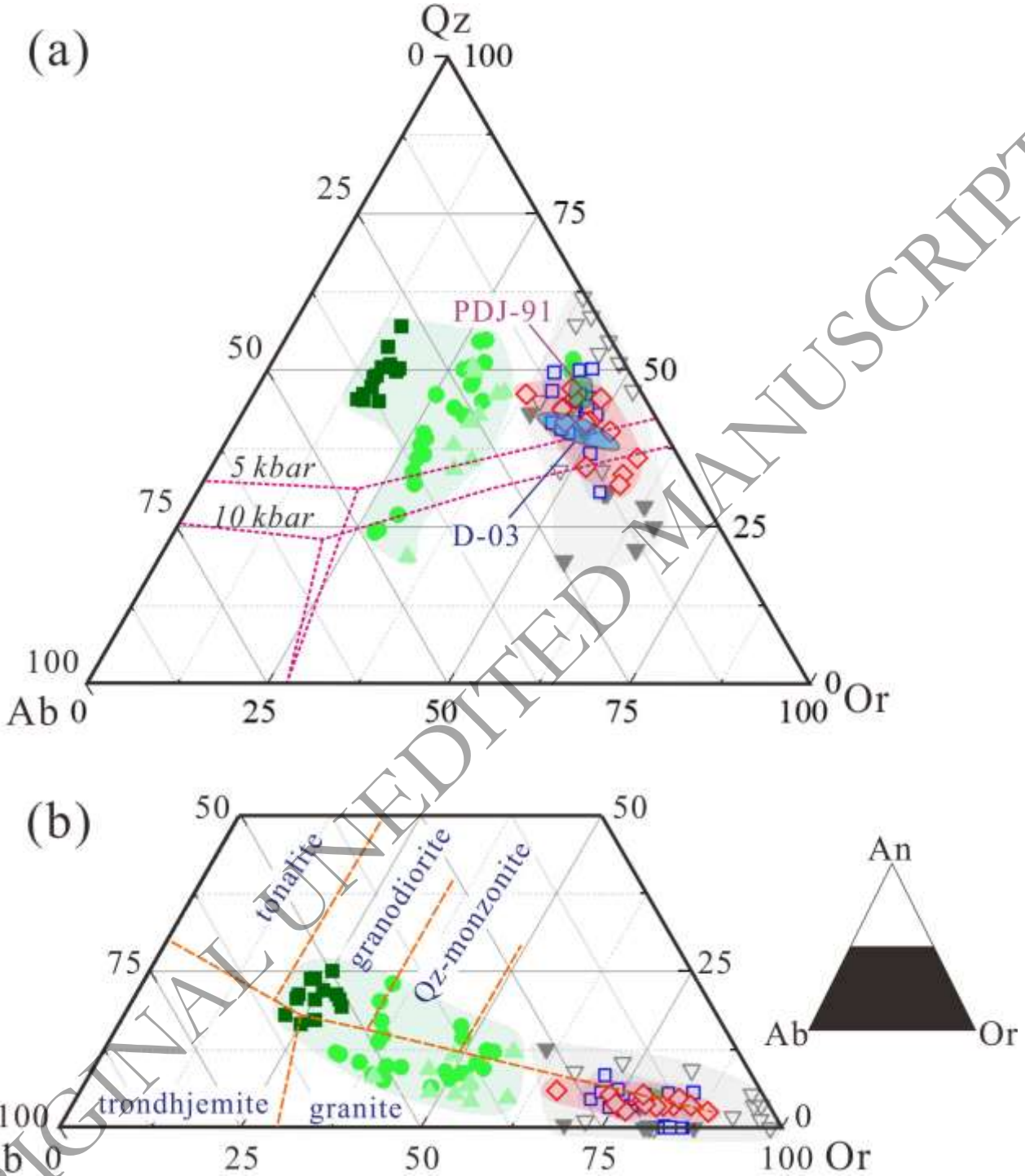

1578

1579

1580

1581

1582

1583

Fig. 11.

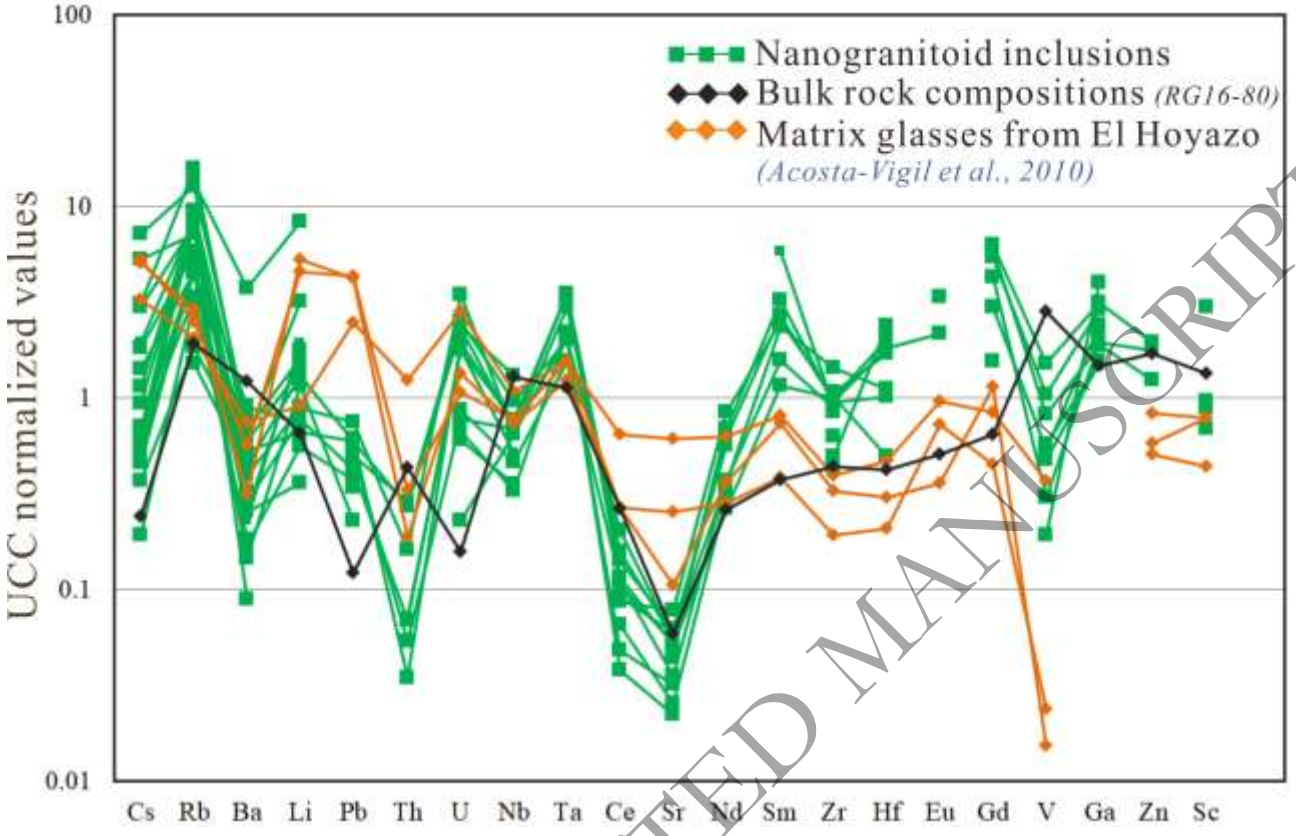

Fig. 12.

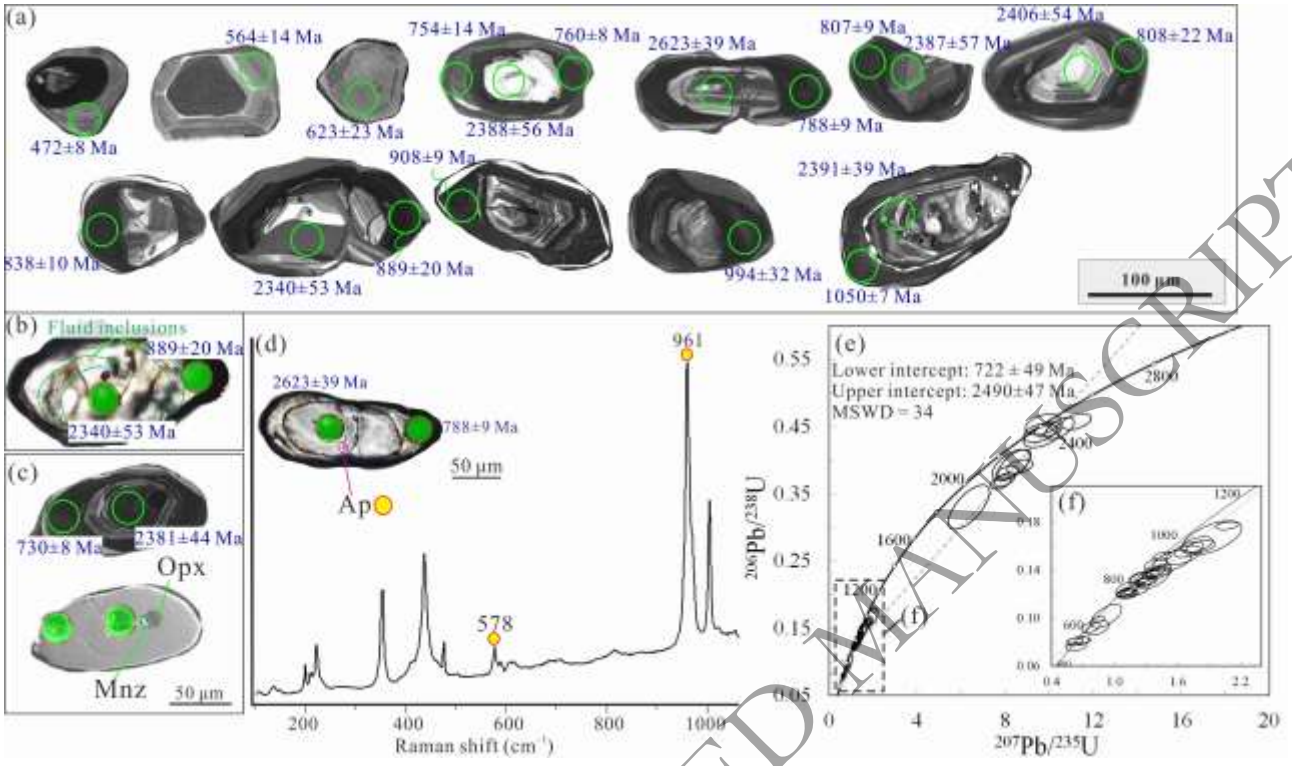

Fig. 13.

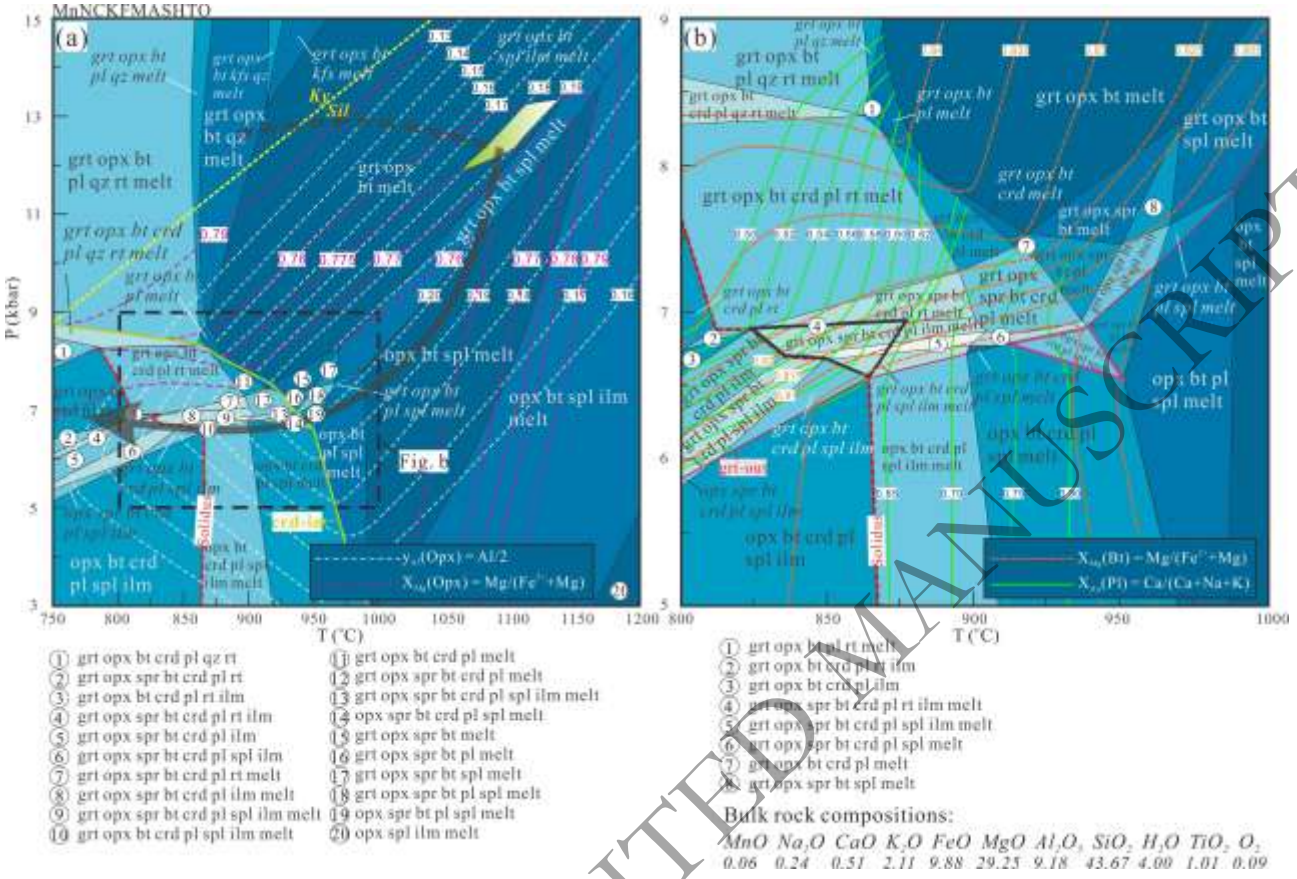

① grt opx bt crd pl qz rt
② grt opx spr bt crd pl rt
③ grt opx bt crd pl rt ilm
④ grt opx spr bt crd pl rt ilm
⑤ grt opx spr bt crd pl ilm
⑥ grt opx spr bt crd pl spl ilm
⑦ grt opx spr bt crd pl rt melt
⑧ grt opx spr bt crd pl ilm melt
⑨ grt opx spr bt crd pl spl ilm melt
⑩ grt opx bt crd pl spl ilm melt
⑪ grt opx bt crd pl melt
⑫ grt opx spr bt crd pl melt
⑬ grt opx spr bt crd pl spl ilm melt
⑭ opx spr bt crd pl spl melt
⑮ grt opx spr bt melt
⑯ grt opx spr bt pl melt
⑰ grt opx spr bt spl melt
⑱ grt opx spr bt pl spl melt
⑲ opx spr bt pl spl melt
⑳ opx spl ilm melt

① grt opx bt pl rt melt
② grt opx bt crd pl qz rt
③ grt opx bt crd pl ilm
④ grt opx spr bt crd pl rt ilm melt
⑤ grt opx spr bt crd pl spl ilm melt
⑥ grt opx spr bt crd pl spl melt
⑦ grt opx bt crd pl melt
⑧ grt opx spr bt spl melt

Bulk rock compositions:

MnO	Na$_2$O	CaO	K$_2$O	FeO	MgO	Al$_2$O$_3$	SiO$_2$	H$_2$O	TiO$_2$	O$_2$
0.06	0.24	0.51	2.11	9.88	29.25	9.18	43.67	4.00	1.01	0.09

Fig. 14.

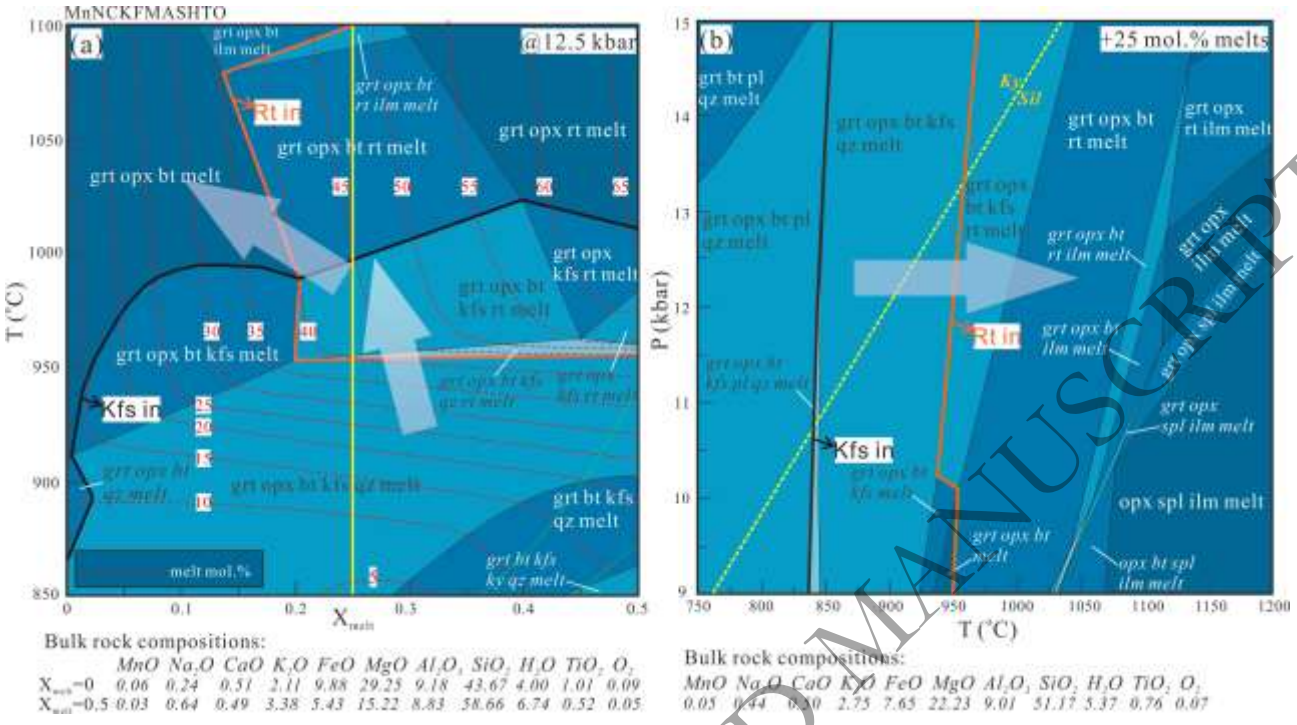

Bulk rock compositions:

	MnO	Na_2O	CaO	K_2O	FeO	MgO	Al_2O_3	SiO_2	H_2O	TiO_2	O_2
X_{melt}=0	0.06	0.24	0.51	2.11	9.88	29.25	9.18	43.67	4.00	1.01	0.09
X_{melt}=0.5	0.03	0.64	0.49	3.38	5.43	15.22	8.83	58.66	6.74	0.52	0.05

Bulk rock compositions:

MnO	Na_2O	CaO	K_2O	FeO	MgO	Al_2O_3	SiO_2	H_2O	TiO_2	O_2
0.05	0.44	0.50	2.75	7.65	22.23	9.01	51.17	5.37	0.76	0.07

1655 **Fig. 15.**

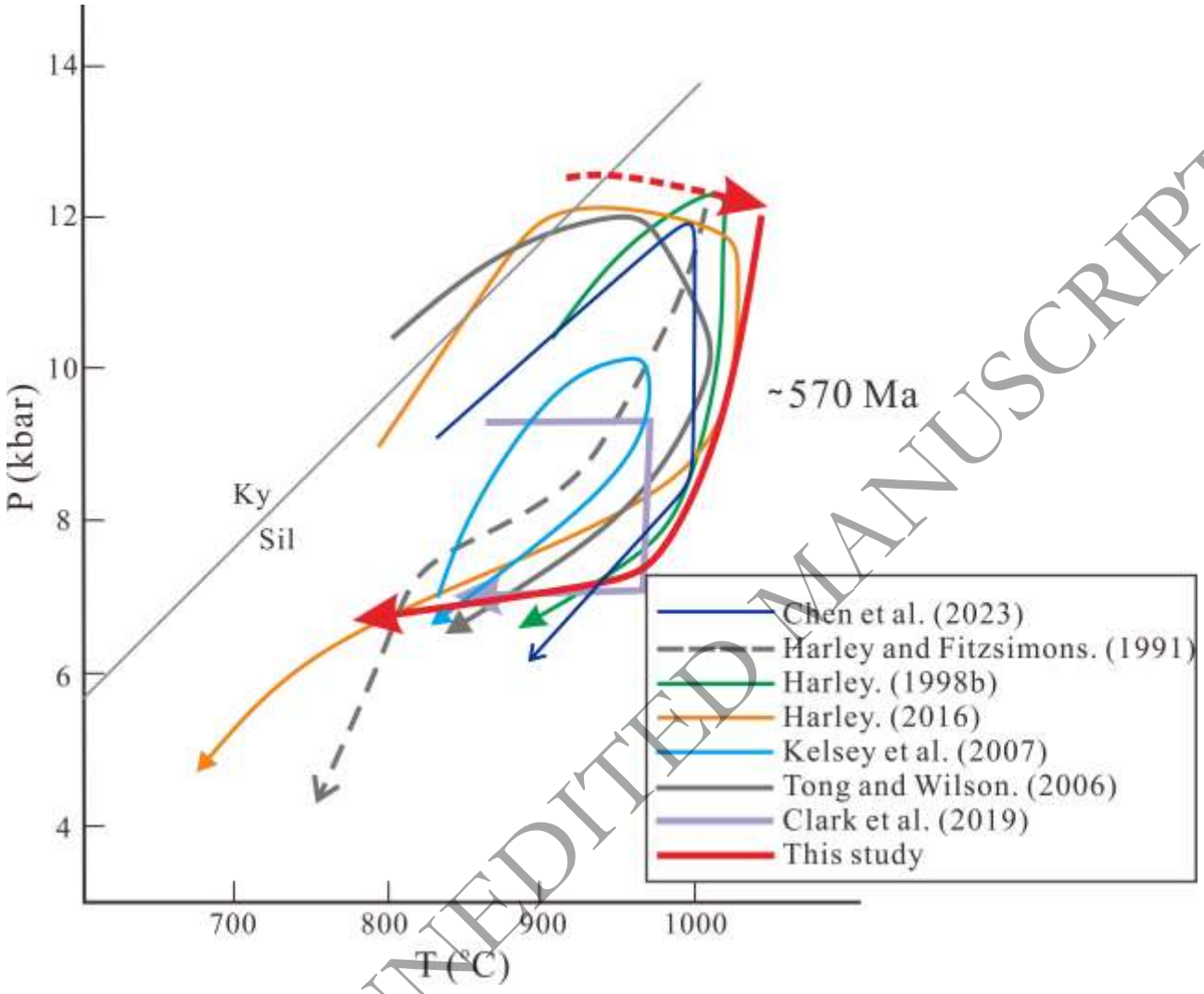

1656